

Analysis of CYGNSS coherent reflectivity over land for the characterization of pan-tropical inundation dynamics

Pierre Zeiger^{a,*}, Frédéric Frappart^b, José Darrozes^c, Catherine Prigent^{d,e}, Carlos Jiménez^{d,e}

^aLaboratoire d'Etudes en Géophysique et Océanographie Spatiale (LEGOS), Université Paul Sabatier (UPS), Toulouse, France

^bInteraction Sol Plante Atmosphère (ISPA), INRAE Bordeaux, Villenave-d'Ornon, France

^cGéosciences Environnement Toulouse (GET), Université Paul Sabatier (UPS), Toulouse, France

^dCNRS, LERMA, Observatoire de Paris, Sorbonne Université, Université PSL, Paris, France

^eEstellus, Paris, France

Abstract

The monitoring of flood and wetland dynamics at global scale is hampered by several limitations, including a reduced data availability in tropical areas due to the presence of clouds affecting visible and infrared imagery, or low spatial and/or temporal resolutions affecting passive and active microwave Earth Observation (EO) data. As a consequence, surface water extent estimates and their temporal variations remain challenging especially in equatorial river basins. Global Navigation Satellite System Reflectometry (GNSS-R) L-band signals recorded onboard Cyclone GNSS (CYGNSS) mission, composed of 8 Low Elevation Orbit (LEO) satellites, provide information on surface properties at high temporal resolution from 2017 up to now. CYGNSS bistatic observations were analyzed for detecting permanent water and seasonal floodplains over the full coverage of the mission, from 40°S to 40°N. We computed CYGNSS reflectivity associated to the coherent component of the received power, that was gridded at 0.1° spatial resolution with a 7-day time sampling afterwards. Several statistical metrics were derived from CYGNSS reflectivity, including the weighted mean and standard deviation, the median and the 90th percentile (respectively Γ_{mean} , Γ_{std} , Γ_{median} and $\Gamma_{90\%}$) in each pixel. These parameters were clustered using the K-means algorithm with an implementation of the Dynamic Time Warping (DTW) similarity measure. They were compared to static inundation maps, and to dynamic estimations of surface water extent both at the global and regional scales, using the Global Inundation Extent from Multi-Satellites (GIEMS) and MODIS-based products. The difference between $\Gamma_{90\%}$ and Γ_{median} shows the best sensitivity to the presence of water. The river streams and lakes are correctly detected, and a strong seasonality is identified in CYGNSS reflectivity over the largest floodplains, with the exception of the Cuvette Centrale of Congo which is covered by dense vegetation. This seasonal reflectivity signal correlates well with inundation maps: Pearson's correlation coefficient between Γ_{median} and surface water extent from both GIEMS and MODIS is over 0.8 in the largest floodplains. The spatial patterns of reflectivity are consistent with static inundation maps: at the time of maximum flooding extent, a spatial correlation coefficient around 0.75 with Γ_{median} is obtained for several basins. We also evaluated the dependence of CYGNSS-derived clusters and reflectivity on the dominant land cover type and on the density of Above Ground Biomass (AGB) in the pixel. On the one hand, misclassifications of flooded pixels were observed over vegetated regions, probably due to uncertainties related to the attenuation by the vegetation in both CYGNSS and reference datasets. On the other hand, flooded pixels with a mean AGB

36 up to ~ 300 Mg/ha were correctly detected with the clustering. High reflectivity values are also observed over
37 rocky soils in arid regions and create false alarms. Finally, strong winds on large lakes cause surface roughness,
38 and lower reflectivity values are observed in this case which weaken the detection of open water. While these
39 constraints are to be taken in account and corrected in a future model, a pan-tropical mapping of surface water
40 extent dynamics using CYGNSS can be envisaged.

41 *Keywords:* GNSS-Reflectometry, CYGNSS, coherent reflectivity, flood dynamics, surface water extent

42 1. Introduction

43 Wetland ecosystems and floodplains play a key role for the management of water and natural resources
44 and for climate change, although they cover only 8% of the land surfaces (Davidson et al., 2018). They temper
45 the water cycles through the regulation of river discharges and the mitigation of floods (Bullock & Acreman,
46 2003; Acreman & Holden, 2013). They are particularly sensitive to climate change, while contributing a lot to
47 the world's greenhouse gases emissions through the global biogeochemical cycles. According to estimations in
48 the literature, wetlands are the source of 20-25% of the world's methane emissions (Bartlett & Harriss, 1993;
49 Whalen, 2005; Bergamaschi et al., 2007; Bloom et al., 2010; Ringeval et al., 2010; Melton et al., 2013; Nisbet
50 et al., 2014; Saunio et al., 2020), and they store 16 to 33% of the soil carbon pool (Maltby & Immirzi, 1993; Page
51 et al., 2011; Mitsch et al., 2013). Beyond the natural biogeochemical cycles, the anthropogenic activity strongly
52 impacts wetlands, and exerts feedback loops along with climate change through the variations of the carbon
53 stocks and methane emissions. Moreover, wetlands are known to be major reserves of biodiversity (Mitra et al.,
54 2005; Junk et al., 2006; Webb et al., 2010). The temporal and spatial variations in inundation extent also affect
55 the propagation of infectious diseases (Kouadio et al., 2012; Suk et al., 2020). All these effects affect the millions
56 of people living worldwide in wetlands and relying on a healthy wetland ecosystem (Maltby & Acreman, 2011).
57 Besides, unprecedented floods and droughts increase the vulnerability in many regions of the world in spite of
58 the improvement of risk management policies (Kreibich et al., 2022). For these aforementioned factors, a better
59 monitoring from regional to global scales of the flood extent and dynamics is needed.

60 Inundation mapping usually depends on remote sensing due to the lack of *in-situ* data and the difficulties to
61 perform measurements in remote regions. Long time-series of inundation extent at 30 m spatial resolution were
62 obtained with the processing of Landsat multispectral images (Pekel et al., 2016), but at the expense of a low
63 temporal resolution. The Moderate Resolution Imaging Spectroradiometer (MODIS) instrument was also used
64 to produce a delineation of flooded area with a 8-day temporal resolution, but with a lower spatial resolution
65 from 250 m to 1 km (Chen et al., 2013; Di Vittorio & Georgakakos, 2018). Nevertheless, while these products
66 provide reliable information on open water bodies, they suffer from limitations due to the presence of clouds in
67 equatorial areas, and are unable to detect water under dense canopies such as the inundated forests present in
68 the Amazon and the Congo basins.

69 Microwave remote sensing is less affected by these limitations in both passive and active domains. The

70 presence of freshwater is responsible for: i) a decrease in the brightness temperature, in passive mode, affecting
71 more sensibly the horizontal than the vertical polarization (Choudhury, 1991; Sippel et al., 1994; Prigent et al.,
72 2001), ii) in active mode, low backscattering over open water and high backscattering in presence of water under
73 vegetation owing to the double-bounce effect for side-looking radar such as Synthetic Aperture Radar (SAR)
74 (Richards et al., 1987), and iii) also in active mode, high backscattering over open water and wetlands for nadir-
75 looking radar altimeters (Frappart et al., 2021), except over large lakes where surface roughness (*e.g.* waves
76 on windy days) can cause a strong scattering. L-band in particular is able to penetrate deeper the vegetation
77 cover than the higher frequency microwave bands. It allows the detection of water under the vegetation even
78 in equatorial basins, in both passive (Parrens et al., 2017) and active (Hess et al., 2003; Betbeder et al., 2014)
79 domains. Nevertheless, major drawbacks limit the use of microwave observations for flood monitoring. First,
80 passive microwave observations have a coarse spatial resolution, generally lower than 25 km, which limits their
81 use for flood monitoring in spite of their quasi-daily temporal repeat. For example, the Soil Moisture and Ocean
82 Salinity (SMOS, Kerr et al. (2001)) and the Soil Moisture Active Passive (SMAP, Entekhabi et al. (2010)) missions
83 measure the brightness temperatures at L-band, with a nominal spatial resolution of several tens of kilometers
84 and a revisit period of 2-3 days. Then, the use of Synthetic Aperture Radar (SAR) active microwave images was
85 also limited by a low temporal sampling before the launch of Sentinel-1, the difficulty to identify the signature
86 of water in complex environments, and the limited availability of L-band images at global scale. Finally, the use
87 of radar altimetry for flood mapping is limited by its acquisition mode along the satellite tracks that does not
88 offer a global coverage of land surfaces and by its low temporal resolutions ranging from 10 to 35 days. As a
89 consequence, most of the studies were limited to regional mapping of the flood dynamics (Hamilton et al., 2004;
90 Kuenzer et al., 2013; Parrens et al., 2017). The combination of multi-satellite information allows to overcome some
91 of these limitations. The Global Inundation Extent Multi-Satellite (GIEMS) product combines information from
92 passive microwave, radar scatterometers, and visible / near-infrared images to account for vegetation effect in
93 the flood detection. It has been providing a continuous monitoring of the wetland dynamics globally, at monthly
94 time scale and $\sim 0.25^\circ$ spatial resolution since 1992 (Prigent et al., 2007, 2020).

95 Global Navigation Satellite System (GNSS) Reflectometry (GNSS-R) onboard satellite platforms can be a
96 great help to improve the spatial and temporal resolutions of wetlands dynamics mapping. It uses the L-band (f
97 = 1.575 GHz for L1) GNSS signals scattered by the Earth's surface, and collected by a receiver as a multistatic mea-
98 surement technique (Martin-Neira, 1993; Zavorotny et al., 2014). In-situ and airborne GNSS-R measurements
99 have shown sensitivity to various oceanic and land geophysical parameters (Ruffini et al., 2004; Cardellach et al.,
100 2011; Egido et al., 2014). Over the last years, satellite missions carrying GNSS-R receivers have been launched
101 and emerge as new tools for global applications.

102 The UK TechDemoSat-1 (TDS-1) mission was a proof of concept of spaceborne GNSS-R measurements. It
103 successfully allowed it to retrieve either oceanic parameters such as sea level and wind speed (Foti et al., 2015;
104 Clarizia et al., 2016), or land geophysical parameters such as soil moisture and vegetation (Camps et al., 2016;

105 Chew et al., 2016). It was followed by the launch of the NASA Cyclone GNSS (CYGNSS) mission, whose 8 Low
106 Earth Orbit (LEO) micro-satellites are designed to monitor the formation of tropical cyclones through wind speed
107 retrieval (Ruf et al., 2016). CYGNSS observations are also collected over land over the pan-tropical area ($\pm 38^\circ$
108 latitude). The design of the mission suits the study of land parameters with a fine spatiotemporal resolution, as
109 each of the 8 satellites records simultaneously 4 observations at a sampling rate of 1 Hz (2 Hz after July 2019).
110 CYGNSS observations are sensitive to the properties of the reflecting surface, including surface roughness, soil
111 moisture (SM), vegetation water content (VWC) and biomass density (Carreno-Luengo et al., 2019). One of the
112 major applications over land of this dataset is soil moisture retrieval with a good accuracy (Root Mean Square
113 Error ranging from 0.04 to 0.07 cm^3/cm^3) (Chew & Small, 2018; Kim & Lakshmi, 2018; Al-Khaldi et al., 2019;
114 Clarizia et al., 2019; Eroglu et al., 2019; Senyurek et al., 2020). It has also been demonstrated that CYGNSS
115 can be used to increase both the spatial and temporal sampling of existing SM products derived from passive
116 microwave sensors (*e.g.*, SMAP, SMOS), that suffer from a lower spatiotemporal resolution (Yan et al., 2020).

117 CYGNSS reflectivity, based on the Delay Doppler Map (DDM) Peak power and metadata used for the cal-
118 ibration of the signal, was also used for identifying flood signatures in the spaceborne GNSS-R observations.
119 In particular, the reflectivity maps show the changes in inundation extent following hurricanes, typhoons or
120 extreme rain events (Chew et al., 2018; Morris et al., 2019; Wan et al., 2019; Ghasemigoudarzi et al., 2020; Ra-
121 jabi et al., 2020). The methodologies mostly consist in an empirical thresholding of the CYGNSS reflectivity
122 or Signal-to-Noise Ratio (SNR), except Ghasemigoudarzi et al. (2020) which used the Random Under-Sampling
123 Boosted (RUSBoost) classification algorithm to identify flooded and non-flooded CYGNSS data. Gerlein-Safdi
124 & Ruf (2019) used CYGNSS to produce annual water masks in the Congo basin, with a 0.1° spatial resolution,
125 using a spatial comparison of one pixel's value with its neighbors and the random walker segmentation method.
126 Then, Gerlein-Safdi et al. (2021) used the same approach temporally, for comparing the monthly mean of a pixel
127 with the average value of its time series. They produced monthly water masks at 0.01° spatial resolution over the
128 Pantanal and Sudd wetlands. Finally, Jensen et al. (2018) studied the relationship between CYGNSS reflectivity,
129 floods and vegetation in tropical wetlands in the hydrographic basin of the Amazon. Based on this analysis,
130 Rodriguez-Alvarez et al. (2019) classified the open water and flooded vegetation over the same study area. Note
131 that all these studies were performed at the regional scale. At larger scale, CYGNSS reflectivity and coherence
132 over flooded areas vary temporally and spatially due to vegetation cover, due to the changes in roughness af-
133 fecting soil and water surfaces (Chew & Small, 2020), and to the bistatic geometry of the acquisition Loria et al.
134 (2020).

135 Recent improvements have been made in the detection of surface water using several indicators of the co-
136 herence of CYGNSS observations. In particular, the raw Intermediate Frequency (IF) data occasionally collected
137 were analyzed in several studies (Li et al., 2021, 2022a; Collett et al., 2022). They are unprocessed signal samples
138 which contain phase information at a high sampling rate, before the incoherent averaging at 1-2 Hz used to
139 derive Level-1 DDM products. Li et al. (2021) calculated the complex DDM and derived a coherent coefficient

140 (CoC) for BeiDou-3 raw IF. They found that a high CoC is highly linked with the presence of water bodies.
141 Li et al. (2022a) proposed a multi-GNSS complex waveform product with a high sampling rate (1000 Hz), that
142 enables the detection of surface water at ~ 100 m spatial resolution along the reflection track. And Collett et al.
143 (2022) showed that the coherence of CYGNSS raw IF samples highly relies on the standing surface water, and
144 if no water body is found in the footprint, coherence is found for saturated soils ($SM \geq 0.45 \text{ cm}^3/\text{cm}^3$) with
145 low large-scale roughness. An entropy-based metric was also proposed by Russo et al. (2022) to characterize the
146 coherence of CYGNSS raw IF. It was very sensitive to open water and floods in forested areas along Yucatan
147 Lake and the Mississippi River (Chapman et al., 2022). An operational and continuous generation of raw IF data
148 at different frequencies and polarizations is planned for the future European Space Agency (ESA) GNSS-R mis-
149 sion, HydroGNSS, of which the detection of surface water is one of the main science objectives (Unwin et al.,
150 2021). But currently, the availability of raw IF data is low compared to CYGNSS Level-1 data, and they are more
151 an object of investigation rather than an operational solution for the monitoring of flood dynamics. For this
152 reason, Al-Khaldi et al. (2021b) gave an estimation of the coherence based on the shape of CYGNSS Level-1
153 DDM. Some pan-tropical water masks were further proposed in Al-Khaldi et al. (2021a) using the aggregation of
154 CYGNSS observations with varying spatio-temporal resolution: 1 km/1 year, 3 km/3 months, and 6 km/2 weeks.
155 At 1-km spatial resolution, the mask is annual at best but the permanent water bodies are well delineated, in-
156 cluding small tributaries of the Amazon and Congo rivers. On the contrary, lower spatial resolution allows a
157 much higher temporal sampling and the detection of flood events.

158 In this study, we focus on CYGNSS reflectivity to map flood dynamics with a 0.1° spatial resolution and
159 a 7-day temporal resolution. The CYGNSS reflectivity time series are classified using a K-means clustering
160 technique with Dynamic Time Warping (DTW) similarity measurement (Müller, 2007), to delineate the flooded
161 areas. Results are compared to reference static and dynamic maps of inundations at global and regional scales,
162 among other ancillary datasets. Section 2 presents the datasets, Section 3 the methodology of this study, while
163 Section 4 and Section 5 show the results and a discussion about the main conclusions of this paper.

164 2. CYGNSS and reference datasets

165 2.1. CYGNSS

166 The CYGNSS mission is composed of 8 LEO micro-satellites covering the pan-tropical area ($\pm 38^\circ$ latitude).
167 Each satellite carries onboard a Delay Doppler Mapping Instrument (DDMI), which is composed of a GPS re-
168 ceiver, nadir-looking antennas for collecting GNSS signals, and a zenith-looking antenna for geolocation pur-
169 pose. The DDMI records simultaneously 4 reflected signals integrated over a second (0.5 s after July, 2019), so
170 the CYGNSS mission provides 32 (64, respectively) observations per second in the area of coverage. The temporal
171 sampling is high, with a median and mean revisit time over a 25 km pixel of 3 hours and 7 hours, respectively
172 (Ruf et al., 2016). With higher spatial resolution, the revisit time increases. Still, substantial improvements in
173 terms of temporal resolution are expected using CYGNSS when compared to monostatic radars.

174 Due to the bistatic configuration of the measurements between an emitting Global Positioning System (GPS)
175 satellite and a receiving CYGNSS observatory, the sampling of CYGNSS observations over the Earth's surface is
176 pseudo-random. The L-band signals ($f = 1.575$ GHz for GPS L1) are emitted by GNSS satellites and received by
177 each of the 8 CYGNSS micro-satellites, with an incidence angle ranging from 0° to $\sim 70^\circ$ and following a Gaus-
178 sian distribution centered on $\sim 30^\circ$. Over the ocean, the reflected GPS signals are dominated by the incoherent
179 component due to an important surface roughness. The spatial resolution is there degraded and wind speed can
180 be estimated with a 25 km spatial resolution and a sub-daily mean revisit time (Clarizia & Ruf, 2016). However,
181 the reflected signals over land can be dominated by the coherent component, in case of the presence of water
182 bodies or areas characterized by a high surface moisture content in the glistening zone, with low surface rough-
183 ness at the scale of the GPS L1 wavelength (19.03 cm). The spatial resolution depends, in that case, on the size
184 of the first Fresnel zone which is larger than ~ 0.6 km \times 0.6 km (the minimum area in the case of a 0° incidence
185 angle) (Eroglu et al., 2019; Rodriguez-Alvarez et al., 2019). The finest theoretical spatial resolution for a CYGNSS
186 observation over flooded regions is therefore ~ 0.6 km \times 6.6 km, with an elongation effect due to the integration
187 of the reflected signals over 1 second (0.5 s, respectively) for observations before (after) July, 2019. Yet, CYGNSS
188 observations are sensitive to the presence of a small fraction of water in the glistening zone, whose contribution
189 dominates the total response of the reflecting surface. The maps of reflectivity over river basins, such as the
190 Amazon, show a strong scattering over small tributaries, down to a few hundred meters.

191 The CYGNSS observables used in this study come from CYGNSS Level 1 science data record files (CYGNSS,
192 2020). They contain the 17x11 Delay Doppler Maps (DDMs) of raw bins and analog scattered power, along
193 with all the parameters used for data processing, *i.e.* the geometry of the acquisition and data flags. We used
194 the version 3.0 of L1 data over one year, from August 1st, 2018 to July 31st, 2019. The observations before
195 July, 2019 are sampled at 1 Hz (2 Hz after), so we assume a ~ 0.6 km \times 6.6 km spatial resolution although the
196 along-track resolution is twice higher for the last month of data. The daily files (one for each CYGNSS satel-
197 lite) are distributed in the Physical Oceanography Distributed Active Archive Center (PODAAC: [https://podaac-
198 opendap.jpl.nasa.gov/opendap/hyrax/allData/cygnss/L1/v3.0/](https://podaac-opendap.jpl.nasa.gov/opendap/hyrax/allData/cygnss/L1/v3.0/)). The CYGNSS DDM of scattered analog power
199 are used in this study, along with quality flags and metadata from the L1 files. The description of the prepro-
200 cessing and analysis of CYGNSS dataset can be found in Section 3 (methodology).

201 2.2. Other sources of data

202 Other data sources were used to analyze and validate the results presented below. They consist in static and
203 dynamic inundation maps available at regional and global scales, land cover thematic map and Above Ground
204 Biomass (AGB).

205 2.2.1. Static inundation maps

206 Two different datasets were considered for a delineation of flooded areas: the Level 3 Global Lakes and
207 Wetlands Database (GLWD-3) at 30" resolution (Lehner & Döll, 2004), and the wetlands maps at 15" (500 m

208 at the Equator) from Tootchi et al. (2019). Note that these two datasets do not provide any temporal variations
209 and are thus static. After some analyzes, the latter was selected because it provides maps of both the Regularly
210 Flooded Wetlands (RFWs, overlapping open water with several inundation datasets) and the Composite Water
211 (CWs) which associates RFWs with Groundwater modelling (GDWs). It is of interest to compare RFWs to CWs
212 maps, because CYGNSS may be sensitive to the groundwater-driven wetlands that represent a considerable
213 source of floods. The CW-WTD product is used as it provides both RFWs areas, and a groundwater wetlands
214 map derived from a direct water table depth (WTD) modeling (Fan et al., 2013).

215 The RFWs in Tootchi et al. (2019) were derived merging 3 inundation datasets, namely the open water and
216 flooded areas extracted from the ESA-CCI Land Cover (see Section 2.2.3), the mean annual maximum water
217 extent from GIEMS-D15 (Fluet-Chouinard et al., 2015), and the maximum surface water from the Joint Research
218 Center (JRC) product (Pekel et al., 2016). It assumes that every single product has observation gaps and should be
219 complemented by the use of other ones. It is particularly the case between the high-resolution JRC maps based
220 on Landsat, and GIEMS-D15 which downscales the coarse 0.25° estimations from GIEMS at 15" resolution. The
221 JRC product is unable to detect water under dense vegetation cover, while GIEMS-D15 is able to detect the
222 floods in tropical or boreal forests. However, GIEMS-D15 is dominant when compared to other products. It
223 represents 55% of the total RFWs areas, and only 10% of its extent is confirmed by either CCI land cover or JRC
224 surface water. As a consequence, the uncertainties of GIEMS are directly propagated in the RFWs dataset. In
225 particular, a recurrent overestimation of Surface Water Extent (SWE) in GIEMS has been found in the Ganges
226 irrigated paddy fields, in the Sahel wetlands, and in coastal areas, due to a confusion between the signals from
227 surface water and wet soils. Also, as the original spatial resolution of GIEMS is 0.25°, the sensitivity to small
228 river streams in several regions, including the Amazon and Congo basins, is found to be low in both GIEMS-D15
229 and Tootchi's RFWs dataset.

230 2.2.2. *Dynamic inundation maps*

231 Few global products exist that provide temporal variations of inundation extent at the global scale. To com-
232 pare with CYGNSS data, we used the Global Inundation Extent from Multi-Satellite version 2 (GIEMS-2) dataset
233 (Prigent et al., 2020). It contains a global estimation of monthly flooded area in a 0.25° grid since 1992. In this
234 study, we have used the new global maps for years 2018 and 2019, matching the times of our CYGNSS dataset.

235 A more precise comparison is performed regionally between CYGNSS observables and multispectral-based
236 flood maps derived from the gridded atmospherically corrected surface reflectances from MODIS, acquired in
237 seven spectral bands from visible/ near infrared (NIR) to shortwave infrared (SWIR). The surface reflectances
238 contained in the MOD09A1 product (8-day binned level 3, version 6) have a spatial resolution of 500 m and
239 a temporal resolution of 8 days. Flood extent maps were generated using the threshold method proposed in
240 Frappart et al. (2018) and Normandin et al. (2018). It is a simplified version of the multi-threshold approach
241 developed by Sakamoto et al. (2007). In this approach, a MODIS pixel is considered fully or partially covered
242 with water if: i) the value of its Enhanced Vegetation Index (EVI) (Huete et al., 1997) is lower or equal to 0.05

243 and the value of its land surface water index (LSWI) (Xiao et al., 2005) is negative or equal to zero, or ii) its EVI
 244 value is lower than 0.3 and the difference between EVI and LSWI is lower than 0.05. This method was used to
 245 produce inundation maps in the Lower Mekong Basin (LMB) in Asia, the Inner Niger Delta (IND) in Africa, and
 246 La Plata basin in South America during the study period.

247 2.2.3. CCI Land Cover

248 The characteristics of CYGNSS reflectivity highly rely on the type of Land Cover (LC) present in the glisten-
 249 ing zone (Carreno-Luengo et al., 2019; Chew & Small, 2020). To analyze the capability of CYGNSS to provide
 250 reliable information on the presence of water over land depending on the LC type, we used global LC maps from
 251 the European Space Agency’s (ESA) Climate Change Initiative (CCI) at 300 m resolution (ESA (2017), available
 252 at <https://www.esa-landcover-cci.org/>). These maps are obtained from 1992 to 2015 using various imagery data,
 253 including the Medium Resolution Imaging Spectrometer (MERIS) and Project for On-Board Autonomy – Veg-
 254 etation (PROBA-V), and applying the GlobCover unsupervised classifier (Defourny et al., 2007). More recent
 255 maps have been produced and validated by the Copernicus Climate Change Service (C3S), so we used the 2019
 256 map which corresponds the best to our CYGNSS time series. Additionally, we aggregated the initial 38 LC types
 257 defined following the United Nations Land Cover Classification System (UN-LCCS) (Di Gregorio, 2016) into 10
 258 general land cover classes, which is summarized in Table 1. Croplands, forests and herbaceous are separated
 259 into dry and flooded regions to study the changes in CYGNSS reflectivity associated to the presence of water.

Table 1: List of the 10 aggregated land cover classes, and the associated class numbers in the CCI LC classification system.

Class numbering	Class name	CCI Land Cover classes associated
LC1	Open water	210
LC2	Cropland non irrigated	10, 11, 12, 30
LC3	Cropland irrigated	20
LC4	Non flooded forest	50, 60, 61, 62, 70, 71, 72, 80, 81, 82, 90
LC5	Flooded forest	160, 170
LC6	Dry shrubs, herbaceous	40, 100, 110, 120, 121, 122, 130
LC7	Flooded shrubs, herbaceous	180
LC8	Bare soils	140, 150, 151, 152, 153, 200, 201, 202
LC9	Snow, ice	220
LC10	Urban	190

260 2.2.4. Above Ground Biomass

261 Dense vegetation layers can attenuate and even extinct the coherent component of GNSS-R signals (Loria
 262 et al., 2020), and the corresponding decrease of CYGNSS reflectivity was also modeled with respect to the Above
 263 Ground Biomass (AGB) of the reflecting surface (Carreno-Luengo et al., 2020). We therefore analysed the distri-
 264 bution of areas detected as flooded and non-flooded using CYGNSS reflectivity, depending on the mean Above
 265 Ground Biomass (AGB) in the pixel. We used the global GlobBiomass AGB maps (Santoro, 2018) which are
 266 given at 1 ha (approximately 3.2 arcsec) spatial resolution for the reference year 2010. It was derived from a set
 267 of observations including the L-band backscatter from ALOS-PALSAR and multiple C-band observations from
 268 Advanced Synthetic Aperture Radar (ASAR) onboard Envisat, with lidar-based metrics from Ice Cloud and Land

269 Elevation Satellite (ICESat), and Landsat reflectances at several bands (Santoro et al., 2021). The study inde-
270 pendently estimated the Growing Stock Volume (GSV) for the backscatters of ALOS-PALSAR and ASAR, which
271 are combined to obtain a more robust dataset and then invert AGB. The AGB maps reproduced well the known
272 spatial patterns with high level of detail. Over the tropics, the comparison with a database of field measurements
273 highlighted a systematic underestimation of AGB in the densest forests. This is due to the low dynamic range
274 of backscatter observations over regions with AGB higher than 250 Mg/ha, and to the unavailability of ASAR
275 GSV estimates which causes the AGB inversion to only rely on ALOS-PALSAR backscatter.

276 2.2.5. *Resampling of the ancillary datasets*

277 All the ancillary datasets have higher spatial resolutions than our 0.1° CYGNSS grid, ranging from ~5100 m
278 to 1 km at the equator. To compare with CYGNSS observables, these data were upscaled into a matching 0.1°
279 grid. For CCI LC, the percentage of each LC class in every pixel was computed. The mean AGB was extracted
280 from GlobBiomass 1 ha spatial resolution dataset. For static and dynamic inundation maps, we calculated the
281 open water and flood extent as a percentage of the pixel surface. A notable exception is GIEMS-2, whose spatial
282 resolution is 0.25°. To compare at the global scale GIEMS vs CYGNSS, we also computed CYGNSS-derived
283 parameters at 0.25° spatial resolution.

284 2.2.6. *Water levels in 2018-2019*

285 We have used water levels derived from radar altimetry as a proxy to estimate the severity of floods in
286 the different river basins further analyzed, during the time span of our study (August 2018 - July 2019). We
287 downloaded the time series of water levels from the Hydroweb database (Crétau et al., 2011; Hydroweb) at
288 several specific locations which are described in the caption of Table 2. We extracted the yearly maximal water
289 heights since 2016 (launch of Sentinel-3A). We then computed the anomaly of 2018-2019 peak water height
290 compared to the average annual maximum, which are listed in Table 2. The relative anomaly represents the
291 anomaly normalized by the average amplitude of seasonal variations, and is also shown. We notice high water
292 levels in the Mekong River (2.96 m over the average, with a relative anomaly of 36.5%), and in South America:
293 0.76 - 0.77 m for the Orinoco and Madeira rivers, with a relative anomaly of 11.1 - 11.5%. This could be due to
294 a weak El Niño in 2018-2019 that may also have affected the Yangtze basin (not shown here). The Parana has
295 a relative anomaly of 42.2% mainly due to a strong decrease of water heights and inundation extent after the
296 severe droughts of the summer 2019, posterior to the time span of our study. For the other basins, the Congo,
297 Ganges and Brahmaputra rivers show low negative anomalies of 0.19 m to 0.39 m (-2.3% to -14.3%), while the
298 Niger shows a positive anomaly of 0.54 m (+7.2%), likely linked to high floods in the Inner Niger Delta. We
299 can also mention the very long-lasting 2019 spring floods along the Mississippi River, that have already been
300 analyzed in several CYGNSS-related studies (Li et al., 2021; Chapman et al., 2022).

Table 2: Anomalies of the 2018-2019 peak water height compare to the average yearly maximum, at the locations listed hereafter. The **Orinoco** River, downstream the Llanos de Orinoco; the **Amazon** River close to its estuary, and the **Madeira** River (one of the biggest tributaries of the Amazon), downstream the confluence between the Beni, Madre de Dios and Mamore rivers; the **Parana** River, after its confluence with Rio Salado; the **Congo** River, after its confluence with the Ubangui; the **Niger** River, downstream the Inner Niger Delta (IND); the **Ganges** and **Brahmaputra** rivers just before their confluence; and finally, the **Mekong** River at the outlet of Tonle Sap.

River	Orinoco	Amazon	Madeira	Parana	Congo	Niger	Ganges	Brahm.	Mekong
Peak anomaly (m)	0.77	-0.03	0.76	1.24	-0.39	0.54	-0.19	-0.3	2.96
Rel. anomaly (%)	11.5	-0.4	11.1	42.2	-14.3	7.2	-2.3	-5.6	36.5

301 3. Methods

302 3.1. Preprocessing of the CYGNSS dataset

303 An overview of the processing chain of CYGNSS data developed in this study is presented in Figure 1. First,
 304 the peak of each CYGNSS DDM in the daily L1 files (see Section 2.1) is extracted and the entire 17x11 L1 DDM is
 305 removed, as a further processing would be very time-consuming. The CYGNSS overland flag is used to remove all
 306 reflections over the oceans, and some other quality flags are applied: *S-band powered up*, *Large spacecraft attitude*
 307 *error*, *Black-body DDM*, *DDM is test pattern*, *Low confidence GPS EIRP estimate*. This set of flags was used in
 308 previous studies to ensure a correct filtering with the removal of the least samples possible (Chew & Small, 2018;
 309 Eroglu et al., 2019). We also tried to apply more constraining masks using all the flags combined in the CYGNSS
 310 overall quality flag with the logical exception of the overland flag (Clarizia et al., 2019; Rodriguez-Alvarez et al.,
 311 2019). However, this latter approach removed a major part of CYGNSS observations over land (Eroglu et al., 2019),
 312 and decreased the performance of land geophysical parameter retrieval with a high spatiotemporal resolution.

313 The CYGNSS L1 algorithms performed an estimation of the specular point location based on a mean sea sur-
 314 face model, which is close to the geoid (Gleason et al., 2019). This can affect the DDMs over land as topography
 315 is not taken into account. Before the end of 2017, data collected over 600 m were of poor quality, which lead
 316 several authors to apply an elevation cutoff (Eroglu et al., 2019; Rodriguez-Alvarez et al., 2019; Yan et al., 2020).
 317 Further versions of the L1 calibration procedures for land reflections include the topography to estimate more
 318 accurately the specular point location (Gleason et al., 2020). For the time span of our study, CYGNSS DDM are
 319 of good quality over a large variety of terrains and elevation ranges, including almost all the wetlands and water
 320 bodies in CYGNSS coverage. Notable exceptions are the Tibetan plateau in the Himalayas, and the Altiplano
 321 in South America (Gleason et al., 2020). Still, the position of the peak power in CYGNSS DDMs is sometimes
 322 shifted due to several factors, including the topography around the specular point. In this study, we filtered the
 323 observations when the peak of the 17x11 DDM is located in the three first and last delay rows as previously
 324 reported (Yan et al., 2020). This corresponds to a quality control affecting a small part (~4%) of the full dataset.

325 3.2. CYGNSS reflectivity

326 The computation of the reflectivity is mostly preferred to the use of the Signal-to-Noise Ratio (SNR) when
 327 analyzing CYGNSS data, as it combines information on the DDM peak power along with other CYGNSS meta-
 328 data useful for the calibration of the signal. The GNSS signals scattered by open water, floodplains and in general
 329 smooth land and ice surfaces are considered to be dominated by the coherent component (Carreno-Luengo et al.,

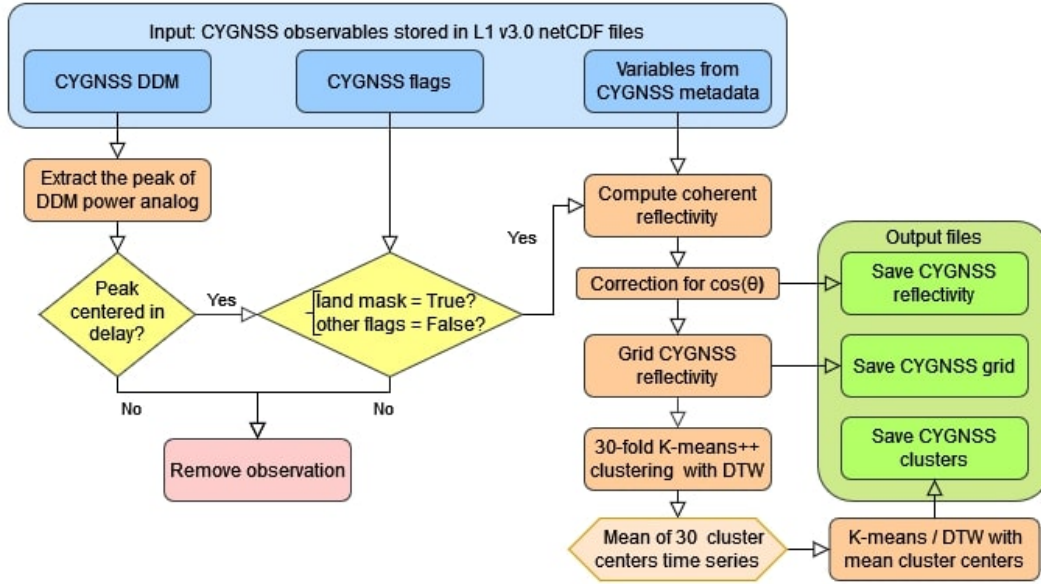


Figure 1: Overview of the processing chain for the analysis and the clustering of CYGNSS observations.

330 2019; Li et al., 2017; Rodriguez-Alvarez et al., 2019). The power ratio (PR) defined in Al-Khaldi et al. (2021a,b) also
 331 highlights high coherent returns with a low diffuse scattering over inland water bodies. In our study, CYGNSS
 332 reflectivity is hence determined using the coherent scattering equation (De Roo & Ulaby, 1994; Gleason et al.,
 333 2020):

$$\Gamma(\theta) = \left(\frac{4\pi}{\lambda}\right)^2 \frac{P_{DDM}(R_r + R_t)^2}{G_r G_t P_t} \quad (1)$$

334 where P_{DDM} is the peak of the DDM analog power, R_r and R_t are the receiver and the transmitter ranges
 335 (distance from the receiver and the transmitter to the specular point), G_r is the receiver antenna gain, $P_t G_t$ is
 336 the GPS Equivalent Isotropically Radiated Power (EIRP), and λ is the GPS L1 signal wavelength (i.e. $\lambda = \lambda_{L1} =$
 337 0.1903 m). P_{DDM} is computed using the 17 delay x 11 Doppler DDMs, while the other variables come from
 338 CYGNSS Level 1 metadata. In Equation (1), the reflectivity depends on the incidence angle (θ) of CYGNSS
 339 observations. In Figure 2, the curves of the mean reflectivity vs. θ are shown without correction (red curve), with
 340 a correction based on $\cos(\theta)$ (in blue), and with a correction based on $\cos^2(\theta)$ (in green). With no correction,
 341 the reflectivity decreases while increasing the incidence angle. With the $\cos(\theta)$ correction, the reflectivity is
 342 \sim constant in all the incidence range, except for $\theta > 68^\circ$ (these values are finally filtered out). With the latter
 343 correction in $\cos^2(\theta)$, the reflectivity increases exponentially with an increasing θ . These corrections based on
 344 $\cos(\theta)$ or $\cos^2(\theta)$ are commonly used in correcting the influence of the incidence angle on SAR backscatter
 345 (Ulaby et al., 1982; Kellndorfer et al., 1998). As a consequence, the reflectivity corrected from the incidence angle
 346 Γ is:

$$\Gamma = \Gamma(\theta = 0^\circ) = \frac{\Gamma(\theta)}{\cos(\theta)} \quad (2)$$

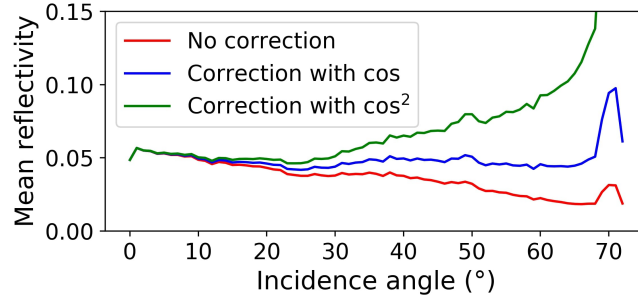


Figure 2: Mean reflectivity vs. the incidence angle for CYGNSS observations without correction for θ , with a correction based on $\cos(\theta)$, and with a correction based on $\cos^2(\theta)$

347 Once CYGNSS reflectivity was computed, these unevenly distributed values were gridded at 0.1° spatial
 348 resolution (~ 11 km at the equator). Several tests were performed to evaluate the best compromise between
 349 spatial and temporal resolutions. For the mapping of variables exhibiting a high temporal variability, such as SM,
 350 a daily time step is preferable and the best spatial resolution associated is 0.25° . For studying flood dynamics, we
 351 preferred to ensure a higher spatial resolution to reduce the confusion between flooded and non-flooded areas.
 352 With a 0.1° grid, a 7-day time sampling can be reached. This observation is consistent with Al-Khaldi et al.
 353 (2021a), who mapped CYGNSS PR at 2 weeks/6 km, 3 months/3 km or 1 year/1 km. Moreover, our grid is based
 354 on a maximum of 32 observations per second (1 Hz sampling of each CYGNSS track). For data after July 2019
 355 the sampling is 2 Hz, so the spatial resolution at weekly time scale could be improved. Finally, an alternative
 356 0.25° grid was also computed to compare CYGNSS reflectivity with the flooded extent from GIEMS-2.

357 Due to the pseudo-random configuration of CYGNSS bistatic observations, some missing values were present
 358 in most of the pixels at specific time steps. A 30-day moving window was applied during the gridding step to
 359 fill these gaps. Figure 3 shows that this process increased the average number of samples per pixel, while the
 360 orbits of CYGNSS satellites ensure more observations at the extreme latitudes, and fewer ones in the equatorial
 361 regions. A 30-day Gaussian window with a standard deviation $\sigma = 7$ days was used to weight the observations.
 362 The weighted mean and standard deviation values of reflectivity per pixel were calculated, which are further
 363 expressed as Γ_{mean} and Γ_{std} in linear units. Other statistical parameters were used to describe the distribution of

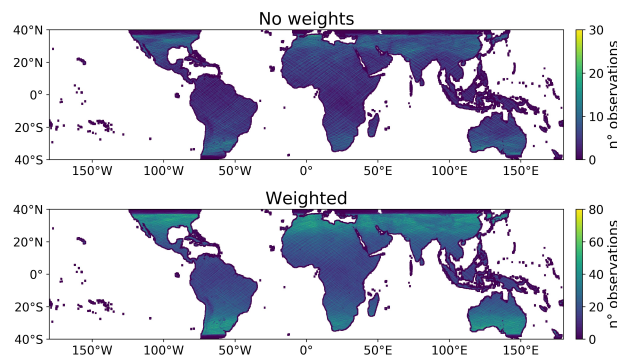


Figure 3: Number of observations per pixel in 7 days, from 2019-01-02 to 2019-01-08. (a) Count without the moving window, (b) count with a moving window and 1-month Gaussian weighting

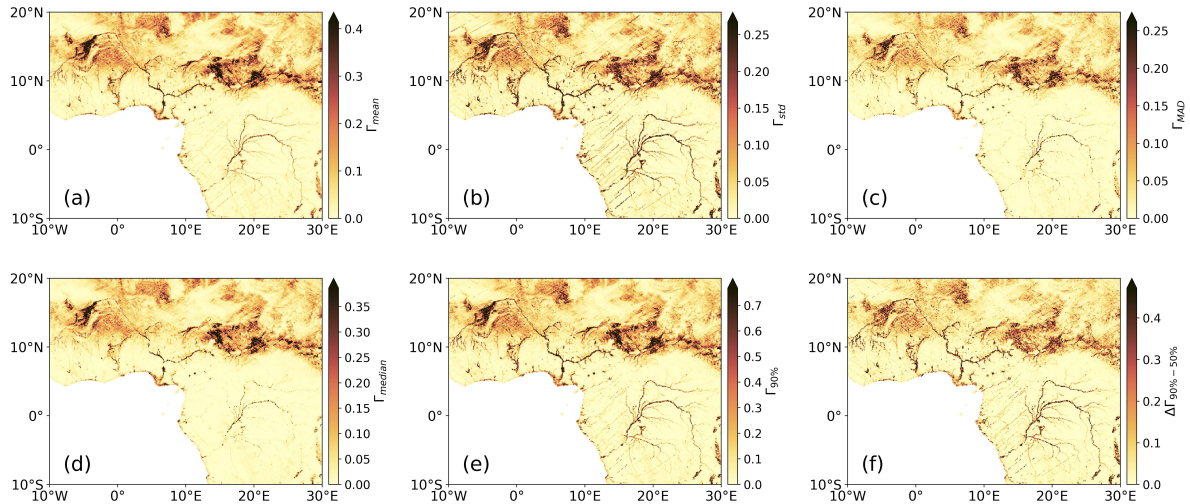


Figure 4: Parameters derived from CYGNSS reflectivity over western and central Africa, with the Congo, Niger and Chad hydrographic basins, at time step 2018-09-05. (a) Γ_{mean} , (b) Γ_{std} , (c) Γ_{MAD} , (d) Γ_{median} , (e) $\Gamma_{90\%}$, (f) $\Gamma_{90\%-50\%}$

364 CYGNSS reflectivity values in each pixel: the median (Γ_{median}), the 90th percentile ($\Gamma_{90\%}$), the median absolute
 365 deviation (MAD, Γ_{MAD}), and the difference between $\Gamma_{90\%}$ and Γ_{median} ($\Gamma_{90\%-50\%} = \Gamma_{90\%} - \Gamma_{median}$). They
 366 were extracted at each time step of the 0.1° grid.

367 A subset of these variables is shown in Figure 4 over western and central Africa, including a major part of
 368 the Congo, Chad and Niger basins, for the first week of September when the Sahel region is affected by floods.
 369 The reflectivity derived from CYGNSS observations is usually high over flooded regions and rivers, which are
 370 smooth reflecting surfaces. All the observables show high values over large wetlands, such as the Inner Niger
 371 Delta (IND) and the floodplains around Lake Chad. Over smaller water bodies, the 0.1° pixels are composed of
 372 a fraction of water with non-inundated areas dominating around. As a consequence, Γ_{median} is low as it comes
 373 from an observation over soils non-covered with water, while $\Gamma_{90\%}$ corresponds to the highest reflectivity values
 374 associated to water bodies. For this reason, the detection of rivers is lower using Γ_{median} and Γ_{MAD} than with
 375 other variables, as it is observed along the streams of the Congo and Niger rivers and their tributaries. The
 376 interest of Γ_{median} and Γ_{MAD} is their robustness to noise, when compared to Γ_{mean} and Γ_{std} , respectively.
 377 Finally, the $\Gamma_{90\%-50\%}$ parameter is relevant, because it discriminates well the river streams (high $\Gamma_{90\%}$ and low
 378 Γ_{median}), the large water bodies and floodplains (high $\Gamma_{90\%}$ and high Γ_{median}), and the non-flooded areas (low
 379 $\Gamma_{90\%}$ and low Γ_{median}).

380 The maps of $\Gamma_{90\%}$ and $\Gamma_{90\%-50\%}$ in the full coverage of CYGNSS mission are shown in Figure 5. The Amazon,
 381 Parana, Congo and Niger Rivers and their tributaries, as well as other smaller streams in the pan-tropical area,
 382 are clearly delineated for both parameters. High reflectivity values are also obtained over the major floodplains
 383 in South America, Africa or Southeast Asia. Finally, a strong specular scattering is observed in the arid regions
 384 over bare soils, such as in the Sahara, the Arabian Peninsula, and Australia (see Section 5.4, discussion). Due
 385 to the homogeneity of the land cover in these areas, high values are obtained for both $\Gamma_{90\%}$ and Γ_{median} . As a
 386 consequence, the difference $\Gamma_{90\%-50\%}$ is low, which improves the separation between water bodies, floodplains

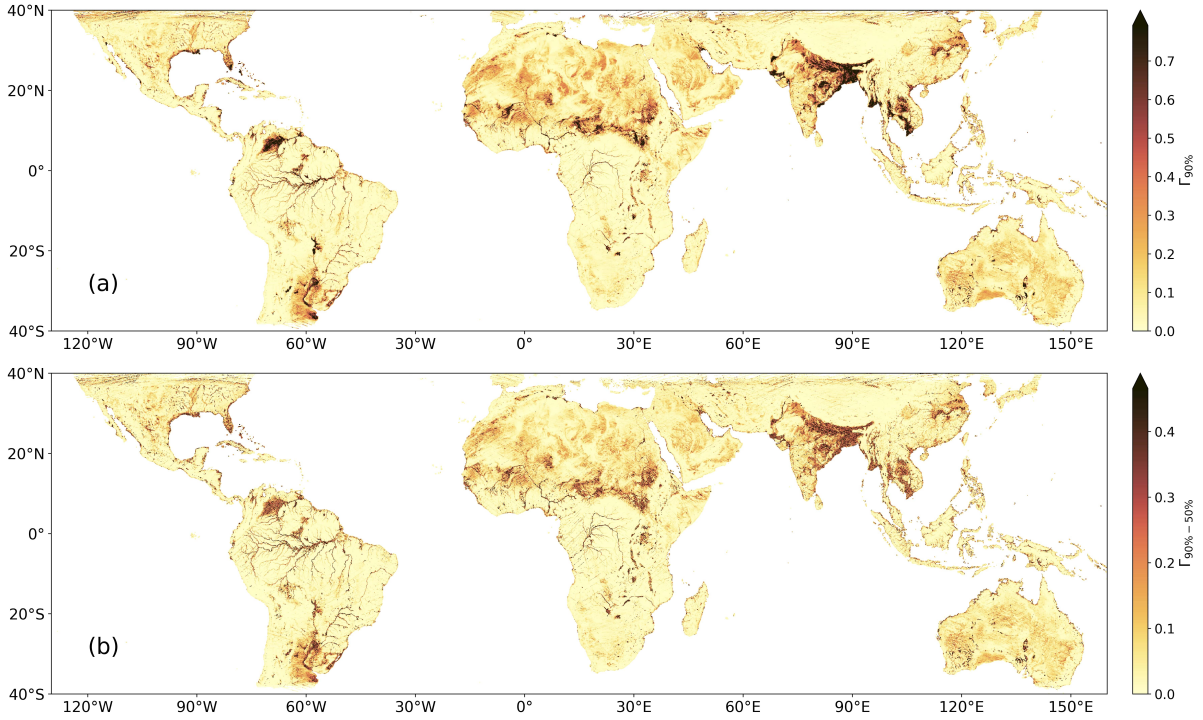


Figure 5: Values at time step 2018-09-05 of CYGNSS-derived parameters: (a) $\Gamma_{90\%}$, (b) $\Gamma_{90\%-50\%}$

387 and bare soils. For all the aforementioned factors, $\Gamma_{90\%-50\%}$ and $\Gamma_{90\%}$ were used along with Γ_{median} for further
 388 analysis in this paper.

389 3.3. Clustering

390 We clustered the CYGNSS-derived parameters Γ_{mean} , Γ_{std} , Γ_{median} , Γ_{MAD} , $\Gamma_{90\%}$ and $\Gamma_{90\%-50\%}$ using the
 391 unsupervised K-means technique (Macqueen, 1967). Starting from an initial set of centroids, it assigns all the
 392 points to the closest cluster center and then calculates the mean value of each cluster. This defines a new set
 393 of centroids, and the algorithm iterates until convergence. The K-means++ method is used to select the initial
 394 cluster centers, as it performs better and provides a good stability of the final solutions (Arthur & Vassilvitskii,
 395 2007). The first centroid is chosen randomly at this step. Then, the other centroids are iteratively determined
 396 between all the dataset points, with a probability equal to the inverse distance between a point and the closest
 397 centroid, the weights being adjusted every iteration. This ensures a stable distribution of the cluster centers that
 398 is representative of the dataset.

399 In this study, we aim to detect inundated areas whatever their seasonality, with a time-series based approach.
 400 This is not possible using the K-means clustering with Euclidean distance, which makes the algorithm extremely
 401 sensitive to shifting and distortion in time. To overcome this limitation of the default K-means algorithm, we
 402 used the Dynamic Time Warping (DTW) similarity measure (Berndt & Clifford, 1994; Müller, 2007) which is
 403 implemented in the python package *tslearn* (Tavenard et al., 2020).

404 Given two time series $X = (x_1, x_2, \dots, x_N)$, $N \in \mathbb{N}$ and $Y = (y_1, y_2, \dots, y_M)$, $M \in \mathbb{N}$, the optimization
 405 problem associated with DTW is formulated as follow:

$$DTW(X, Y) = \min_{\pi} \sqrt{\sum_{(i,j) \in \pi} d(x_i, y_j)} \quad (3)$$

406 where $\pi = [\pi_0, \pi_1, \dots, \pi_K]$ with $\pi_k = (i_k, j_k)$ is called a warping path, and $d(\cdot, \cdot)$ is a distance metric (by
407 default the Euclidean distance is used). The warping path must satisfy the following conditions:

- 408 (i) Boundary condition: $\pi_0 = (1, 1)$ and $\pi_K = (N, M)$
- 409 (ii) Monotonicity condition: $i_k \leq i_{k+1}$ and $j_k \leq j_{k+1}, \forall k \in [1, K - 1]$
- 410 (iii) Step size condition: $i_{k+1} - i_k \leq 1$ and $j_{k+1} - j_k \leq 1, \forall k \in [1, K - 1]$

411 The minimization of all the potential warping paths according to the distance metric $d(\cdot, \cdot)$ results in the
412 optimal warping path, which is here expressed as $DTW(X, Y)$. The optimal warping path is computed between
413 the K-means cluster centers and every pixel at each iteration of the algorithm, and permits a shift and a distortion
414 in time between the time series. This makes the DTW similarity measure well suited for our study. When applied
415 to the detection of inundations, it allows to identify similarities in flood patterns from distinct regions of the
416 world, with differences in phase and intensity. One limitation in our case is the boundary condition (i), because
417 we only use one year of CYGNSS data to detect floods with a yearly seasonal cycle. Thus, we implemented
418 in our methodology a padding of the CYGNSS dataset over 3 consecutive years to limit the boundary effects.
419 The evaluation of a 3 to 5-year dataset of CYGNSS observations would be optimal. However, the choice of a
420 padding was driven by constraints on our computation capacities. It assumes a constant seasonality, which
421 seems reasonable. The methodology could still be extended to the full 5-year dataset of CYGNSS in the future.

422 The choice of an optimal number of centroids in the K-means algorithm can be discussed. Due to the impor-
423 tant computational resources needed by the DTW similarity measure, we were not able to calculate any metric
424 as the Calinski-Harabasz score (Calinski & Harabasz, 1974) and the Silhouette score (Rousseeuw, 1987) with
425 this version of the algorithm. We finally adopted an empirical approach for the determination of the optimal
426 number of clusters, and we tested our methodology with a number of classes ranging from 2 to 8. The results are
427 evaluated graphically with the maps and time series of labelled pixels, and numerically with confusion matri-
428 ces between CYGNSS clusters and flood reference classes based on Tootchi et al. (2019). We also evaluated the
429 capability of each of the 6 CYGNSS-based parameters presented in Figure 4 to detect floods and water bodies,
430 either individually or associated to each-other. The most interesting results are obtained using $\Gamma_{90\% - 50\%}$, which
431 associates the information of Γ_{median} and $\Gamma_{90\%}$ into a unique variable. We therefore only present the results
432 based on this parameter, although all the configurations were evaluated.

433 3.4. Sensitivity to the choice of initial centroids

434 Although the use of K-means++ algorithm produced stabler results than a pure random selection of the
435 initial centroids, some differences were observed between successive versions of the clustering. We computed

436 30 times the K-means++ / DTW algorithm with 4 clusters and the $\Gamma_{90\%-50\%}$ parameter (the best configuration,
437 see Section 4), to perform a sensitivity analysis. We extracted the inertia (sum of distances of samples to their
438 closest cluster centers) at each iteration. We also calculated the percentage of correspondence between the
439 labelled pixels from every pair of distinct clustering results. If the correspondence reaches 100%, the two versions
440 are exactly the same. Table 3 presents some statistical parameters for both the inertia and the correspondence,
441 which are the mean, median, min, max and std values. As can be seen, the inertia covers a very low dynamic
442 range from 0.1005 to 0.1055 with a standard deviation of 10^{-3} , indicating that the algorithm converges toward
443 similar solutions, whatever the choice of the initial centroids by the K-means++ method. The dynamic range
444 of the correspondence is higher ($\sim 80 - 99\%$), with a median value of 94.57% and a standard deviation of
445 4.07%, respectively. The results are usually quite stable, in the range of 92%-99%, with the exception of few ones.
446 Graphically, the different solutions found in 30 iterations also look very consistent.

Table 3: Sensitivity of the clustering result to the choice of initial centroids by the K-means++ algorithm. We calculated the inertia of each clustering, and the correspondence between every pair of distinct clustering results. We present here the mean, median, minimum, maximum and standard deviation values of both parameters.

Result	mean	median	min	max	std
Inertia	0.1027	0.1026	0.1005	0.1055	0.0010
Correspondence (%)	93.76	94.64	80.26	98.78	4.01

447 We finally achieved a second round of the K-means / DTW clustering, which was based on the results of
448 the sensitivity analysis. There, the 4 initial centroids were obtained by averaging the cluster centers of the 30
449 outputs obtained with K-means++ initialization. This step permits to obtain a robust classification that does not
450 vary through the random choice of the initial centroids, but is still based on unsupervised techniques. All the
451 clustering results presented in the following section are computed that way.

452 4. Results

453 4.1. Clustering of CYGNSS reflectivity

454 We clustered the CYGNSS $\Gamma_{90\%-50\%}$ parameter with a number of classes k ranging from 2 to 8, in order
455 to empirically determine the optimal number of clusters. For all the configurations, we plotted the maps of
456 labelled pixels and we calculated a confusion matrix between the CYGNSS clusters and a reference set of water
457 and inundation classes derived from RFWs maps (Tootchi et al., 2019). The definition of the reference classes
458 is detailed in Table 4. Open water is grouped into a single class with a threshold at 10% corresponding to the
459 empirical breaking point of permanent water (class A) vs. dry land (class E). Other classes, *i.e.* high floods (class
460 B, maximum surface water extent $SWE \geq 80\%$), medium floods (class C, $40\% \leq SW < 80\%$) and low floods (class
461 D, $5\% \leq SW < 40\%$), correspond to different levels of maximum inundation extent per pixel.

462 For a low number of clusters (*i.e.*, $k = 2$ or $k = 3$), the clustering problem was highly simplified as the
463 separation of flooded vs. dry areas, according to the average values of $\Gamma_{90\%-50\%}$ related to the intensity of
464 inundation. The results with $k = 4$ are more interesting, as the additional cluster represents the pixels in

Table 4: Definition of the reference classes of open water and floods with the RFWs dataset (Tootchi et al., 2019).

Reference class	Name / interpretation	Open water %	Seasonal water %
A	Permanent water	$\geq 10\%$	-
B	High floods	$< 10\%$	$\geq 80\%$
C	Medium floods	$< 10\%$	$\geq 40\%$ and $< 80\%$
D	Low floods	$< 10\%$	$\geq 5\%$ and $< 40\%$
E	Non flooded areas	$< 10\%$	$< 5\%$

465 floodplains with a strong seasonal cycle during the year. Finally, the results with $k \geq 5$ show an increasing
 466 confusion between one or several clusters associated to both seasonal flood patterns and permanent water. The
 467 choice of $k = 4$ as the optimal configuration was based on both statistical outputs (confusion matrices), and
 468 graphical interpretation of the clustering results.

469 We present the confusion matrix and the results of the clustering with $\Gamma_{90\%-50\%}$ and $k = 4$ in Table 5 and
 470 Figure 6, respectively. The output clusters are referred as C1, C2, C3 and C4 from the lowest to the highest
 471 average $\Gamma_{90\%-50\%}$ values. The map of labelled pixels is shown in Figure 6.a, while Figure 6.b-j represent the
 472 average time series of $\Gamma_{90\%-50\%}$ and $\Gamma_{90\%}$ for the pixels classified in C3 and C4, over 9 large river basins.
 473 The cluster C4 (in blue in Figure 6) exhibits high values for both $\Gamma_{90\%-50\%}$ and $\Gamma_{90\%}$ over the entire time
 474 series, associated to a seasonality in phase with variations of inundation extent. The pixels in C4 are located
 475 on lakes, river streams such as the Amazon, Parana, Niger and Congo Rivers, and also some large floodplains
 476 with permanent water or high SM throughout the year. This cluster represents only 4.4% of the total labelled
 477 pixels, but includes 58.8% of the reference class A (open water), 32.7% of class B (high floods) and 19.0% of class
 478 C (medium floods), according to the results in Table 5 (percentage values in red).

Table 5: Confusion matrix between reference classes A to E defined in Table 4 and CYGNSS clusters C1-4 shown in Figure 6. For each cell in the table, the proportion of pixels in this cell vs. the total number of pixels from the reference class (column Total) is shown in red, and the proportion vs. the total number of pixels from the CYGNSS cluster (line All) is shown in blue. As an example, the box A / C1 contains 9.6% of the total pixels in reference class A, and 0.2% of all the pixels in CYGNSS cluster C1.

	C1	C2	C3	C4	Total
A	804 (9.6%, 0.2%)	650 (7.8%, 0.4%)	1993 (23.8%, 3.3%)	4911 (58.8%, 15.5%)	8358 (1.2%)
B	2150 (9.5%, 0.4%)	3861 (17.1%, 2.6%)	9150 (40.6%, 15.2%)	7353 (32.7%, 23.3%)	22514 (3.1%)
C	8037 (21.9%, 1.7%)	10620 (28.9%, 7.1%)	11121 (30.3%, 18.4%)	6980 (19.0%, 22.1%)	36758 (5.1%)
D	41226 (43.3%, 8.5%)	28782 (30.2%, 19.2%)	16963 (17.8%, 28.1%)	8211 (8.6%, 26.0%)	95182 (13.2%)
E	430066 (76.7%, 89.2%)	105628 (18.8%, 70.6%)	21092 (3.8%, 35.0%)	4160 (0.7%, 13.2%)	560946 (77.5%)
All	482283 (66.6%)	149541 (20.7%)	60319 (8.3%)	31615 (4.4%)	723758

479 Then, the cluster C3 in dark green shows variations from low to high values of $\Gamma_{90\%-50\%}$ and $\Gamma_{90\%}$, with
 480 a seasonal trend particularly visible in $\Gamma_{90\%}$. The pixels in C3 are located on the major floodplains in the pan-
 481 tropical area: the Llanos de Orinoco, Llanos de Mojos, Rio Branco, Pantanal and Parana floodplains in South
 482 America, the Inner Niger Delta (IND), Lake Chad and along the Nile in Africa, the Ganges-Brahmaputra, Indus,
 483 Irrawaddy, Yangtze and Mekong basins in Asia. The seasonality in C3 exhibits maximum values of $\Gamma_{90\%-50\%}$
 484 and $\Gamma_{90\%}$ during summer in the Orinoco (Figure 6.b), Niger (Figure 6.e), Lake Chad (Figure 6.f) and Ganges-
 485 Brahmaputra (Figure 6.h) basins, all located in the northern hemisphere. On the contrary, in the Amazon (Fig-
 486 ure 6.c, across the equator) and Parana (Figure 6.d, in the southern hemisphere) basins, the maximum values

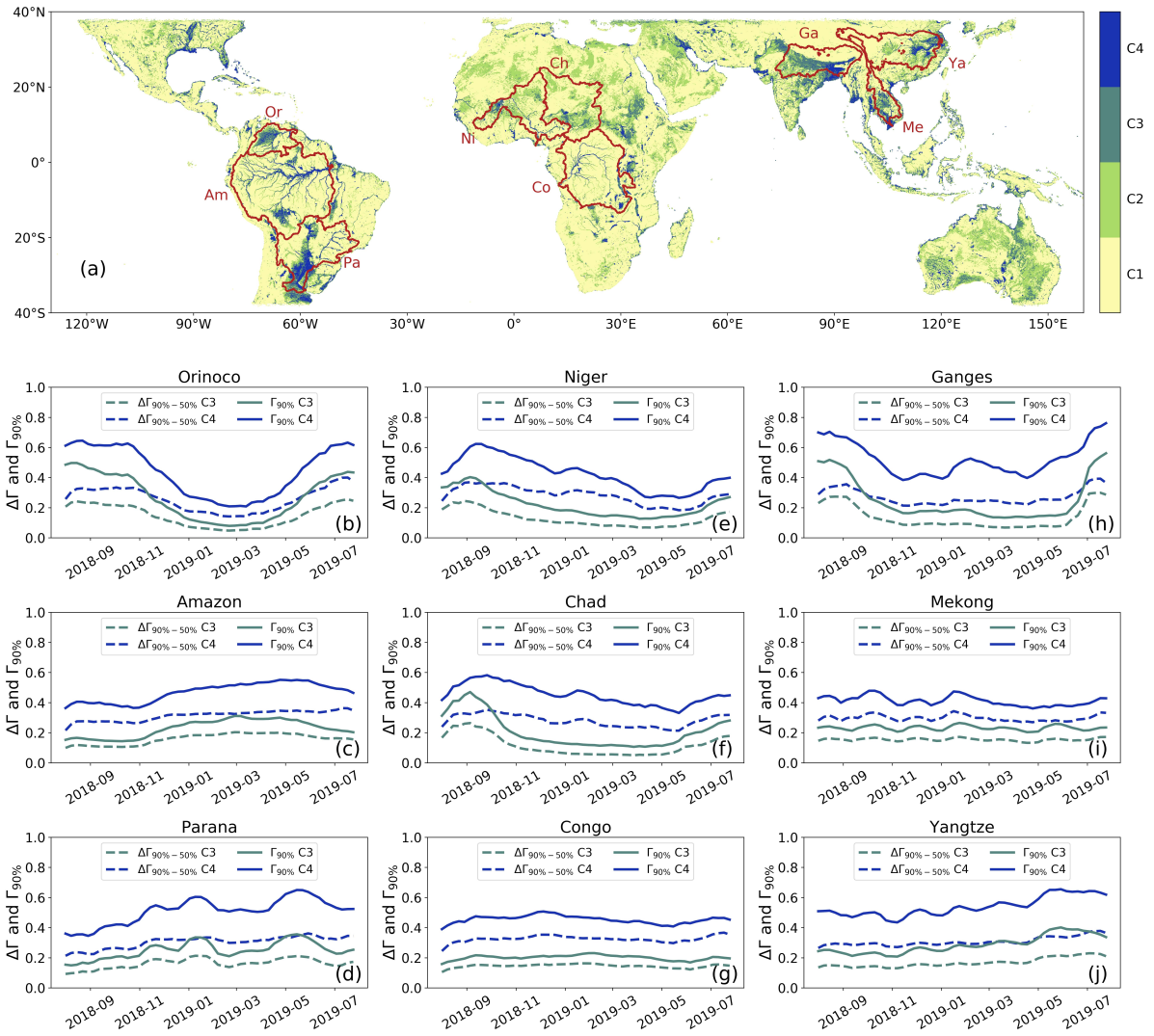


Figure 6: Clustering of $\Delta\Gamma = \Gamma_{90\% - 50\%}$ with 4 clusters. (a) Map of the labelled CYGNSS pixels using the K-means / DTW algorithm with $k = 4$. (b-j) Average time series of $\Gamma_{90\% - 50\%}$ and $\Gamma_{90\%}$ for clusters C3 and C4 in 9 large river basins: (b) Orinoco, (c) Amazon, (d) Parana / La Plata, (e) Niger, (f) Lake Chad, (g) Congo, (h) Ganges-Brahmaputra, (i) Mekong, and (j) Yangtze. The boundaries of all the 9 basins are superposed with the map of labelled clusters in (a), with the two first letters of the basin name allowing its identification.

487 in C3 for $\Gamma_{90\% - 50\%}$ and $\Gamma_{90\%}$ are obtained during spring. This validates the use of the DTW similarity mea-
 488 surement to cluster $\Gamma_{90\% - 50\%}$ time series, for the extraction of flooded areas with distinct temporal cycles. For
 489 statistical results, C3 represents 8.3% of the total labelled pixels, and includes 23.8% of the reference class A,
 490 40.6% of class B, 30.3% of class C, and 17.8% of class D (low floods) according to Table 5 (values in red). If we
 491 merge the two clusters C3 and C4, their combination represent only 12.7% of the world pixels, but 82.6% and
 492 73.3% of the reference classes A and B, respectively. Thus, the identification of open water and flood signatures
 493 in CYGNSS reflectivity is highly reliable.

494 The cluster C2 has medium values of $\Gamma_{90\% - 50\%}$ (not shown) corresponding to either water bodies and pixels
 495 with a fraction of water but not totally flooded (28.9% and 30.2% of classes C and D, respectively), or non-flooded
 496 regions from the reference class E. In Figure 6.a, it is possible to locate C2 mainly over bare soils in arid regions
 497 such as the Sahara, the Arabian Peninsula and Australia. Finally, the cluster C1 is dominant (66.6% of the labelled

498 pixels), and is interpreted as non-flooded areas although it includes about 9.5% of the pixels from both reference
499 classes A and B.

500 In fact, some confusions are identified in the clustering despite a strong sensitivity to the presence of wa-
501 ter. First, the pixels from reference class E which are theoretically non-inundated, represent 13.2% and 35.0%
502 respectively (values in blue in Table 5) of the clusters C4 and C3, exhibiting the highest $\Gamma_{90\%-50\%}$ values. Then,
503 the cluster C2 is a mix of pixels located over flooded and non-flooded regions. This is mainly due to a strong
504 specular scattering over rocky bare soils (see the Section 5.4, discussion for more details). And lastly, while the
505 open water and high floods (classes A and B) are well detected, it is not the case for the medium and low floods
506 (classes C and D). They are associated to a mixing of wetlands and dry areas, and are quite equally divided into
507 the 4 CYGNSS clusters. All these misclassifications can be related to: i) the influence of other factors such as
508 the vegetation, SM, elevation, topography and small-scale roughness in the GNSS-R signals over land, ii) the
509 heterogeneity of land cover and flood occurrence inside a CYGNSS pixel at 0.1° spatial resolution, and iii) errors
510 in the definition of the reference classes, either due to the choice of our thresholds or to the high uncertainties
511 associated to the RFWs product from Tootchi et al. (2019) itself (see Section 2.2.1 for more details).

512 4.2. Comparison with ancillary datasets

513 We have used CCI Land Cover maps and Tootchi's RFWs dataset described in Section 2 to investigate how
514 the land cover changes and the occurrence of water influence CYGNSS-derived clusters. In Figure 7, these
515 parameters are analyzed over three complementary study areas: the northern part of South America, between
516 20°S and 10°N, encompassing the Amazon, Orinoco, Tocantins and São Francisco river basins, as well as the
517 Pantanal floodplains, the Titicaca and Poopó lakes (Figure 7.a1-5); Western and Central Africa around the gulf
518 of Guinea, between 5°S and 20°N, including the Niger River Basin, Lake Chad and the Cuvette Centrale of
519 Congo (Figure 7.b1-5); the Indian subcontinent including the Ganges-Brahmaputra and the Irrawaddy basins
520 (Figure 7.c1-5). These regions include all types of land cover present in the pan-tropical area, e.g. equatorial
521 forests, floodplains under canopy layers or with herbaceous covers, croplands irrigated or not, savannas, bare
522 soils, high mountain ranges.

523 There is a good correspondence between the DTW clusters C3 and C4 in Figure 7.a1-c1 corresponding to
524 areas with high values of $\Gamma_{90\%}$ and $\Gamma_{90\%-50\%}$, and the reference map of water extent derived from Tootchi
525 et al. (2019) in Figure 7.a2-c2. The delineation of permanent water bodies and in particular the streams of the
526 Amazon, Congo and Niger Rivers as well as their tributaries is clear, mainly in cluster C4. The most extensive
527 floodplains are also detected in C3 and C4. In South America, we identify the Llanos in the Northeast Orinoco
528 Basin (around 7°N and 70°W), Llanos de Mojos in the Southwest Amazon Basin (15°S and 65°W), the Rio Branco
529 floodplain in the northern Amazon Basin (0° and 63°W), and the Pantanal floodplains (18°S and 58°W). In Africa,
530 the IND (15°N and 5°W) and the floodplains around Lake Chad (10°N and 15°E) are well detected, but the Cuvette
531 Centrale of Congo (0° and 17°E) is not. In the Indian subcontinent, a strong seasonal signal is obtained and mainly
532 associated to C3 over the irrigated croplands (land cover class LC3 in cyan) along the Ganges plain. The Ganges-

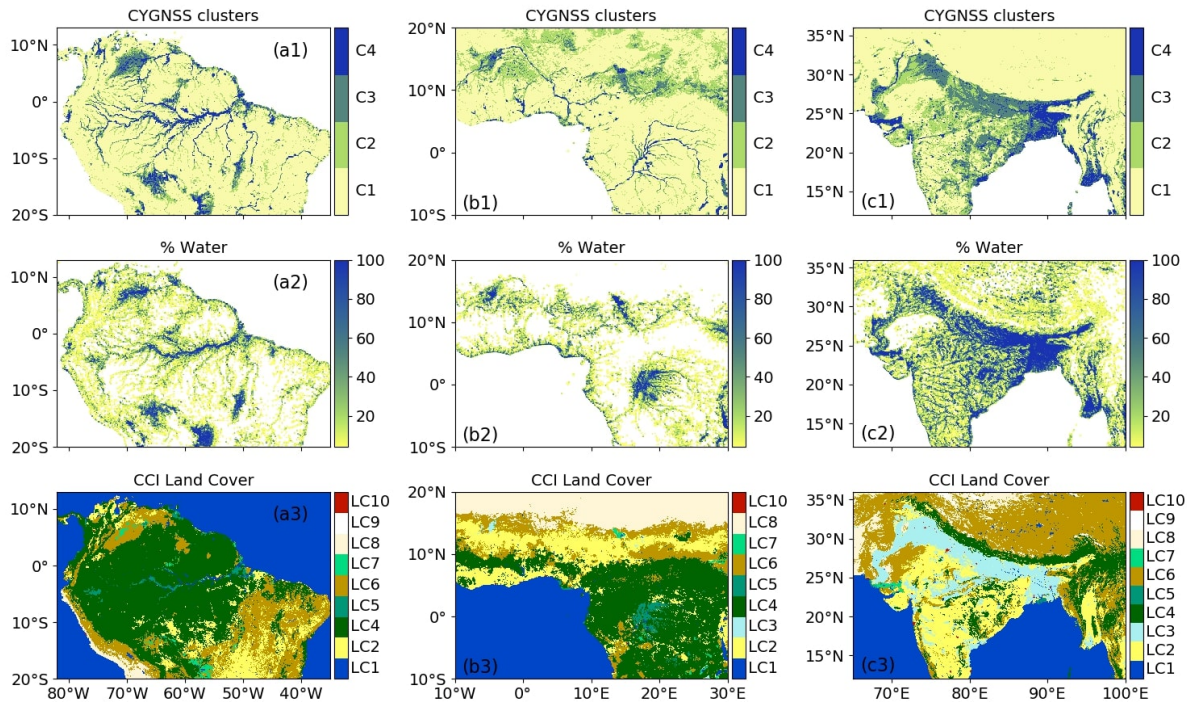


Figure 7: Comparison of CYGNSS-derived parameters with ancillary datasets over the northern part of South America (a1-3), Western and Central Africa with the Gulf of Guinea (b1-3), and the Indian subcontinent (c1-3). (a1, b1, c1) CYGNSS clusters, (a2, b2, c2) Percentage of water from Tootchi's RFWs maps (Tootchi et al., 2019), (a3, b3, c3) CCI Land Cover with the 10 aggregated classes defined in Table 1

533 Brahmaputra delta, the Irrawaddy River and their tributaries are also well delineated. The interesting point is
 534 that CYGNSS reflectivity maps show a good ability for monitoring heavy seasonal floods, almost regardless of
 535 the LC types. Yet, the densest canopies cause a strong attenuation or a diffusion of the L-band signal. Over
 536 the Cuvette Centrale of Congo (bottom right in Figure 7.b1-3), we notice that CYGNSS likely underestimates
 537 the presence of floods nearby the streams of the Congo and Ubangi Rivers, if we refer to the RFWs dataset.
 538 Also, several lakes and wet areas in the Tibetan plateau in the upper right corner of Figure 7.c1-3 are not even
 539 detected using CYGNSS. The estimation of the specular point location is of poor confidence over the Tibetan
 540 plateau, which is about 5000 m high (Gleason et al., 2020), thus CYGNSS DDMs are not centered on the specular
 541 point and likely contain only thermal noise and diffuse scattering from surrounding areas.

542 The same datasets are analyzed in Figure 8 but on smaller regions, with a focus on some significant water
 543 bodies. Figure 8.a1-5 is centered on Lake Titicaca (3812 m high), Figure 8.b1-5 on Lake Victoria (1133 m high),
 544 Figure 8.c1-5 on the Lower Mekong Basin including Tonle Sap, the largest lake of south east Asia, and Figure 8.d1-
 545 5 on Lake Chad (both at low elevation). Several indications must be highlighted in Figure 8. First, all water bodies
 546 are detected using CYGNSS, and mostly classified in C3 or C4 by the DTW clustering. These classes include a
 547 part of Lake Titicaca, Lake Poopó and the Salar de Uyuni located on the Altiplano at high elevation. Although
 548 the estimation of specular point location in this region has low confidence, a strong returned power is often
 549 observed with coherent reflection conditions. Then, it appears that the Tonle Sap and Lake Chad are classified
 550 in C4, while the surrounding floodplains are mostly classified in C3. This shows an example of the separation
 551 of permanent water vs. seasonal floods using CYGNSS. The Delta of Mekong mainly belongs to C4, likely due

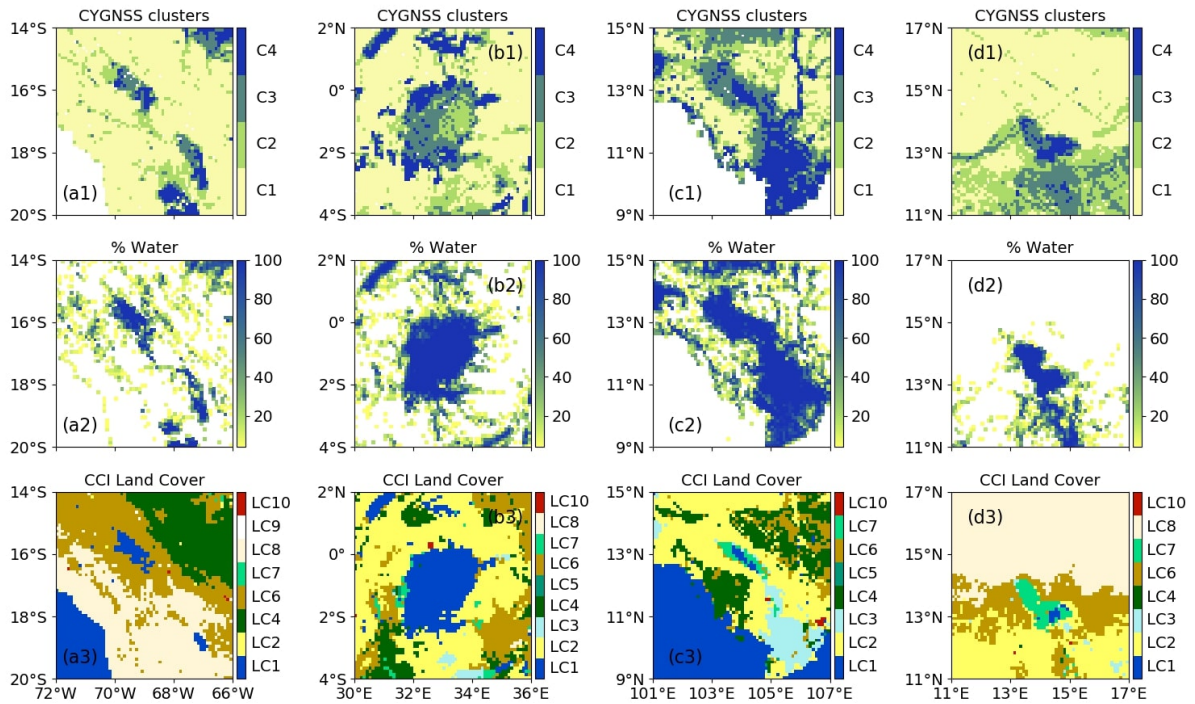


Figure 8: Comparison of CYGNSS-derived parameters with ancillary datasets over small subsets centered on water bodies. **(a1-3)** Portion of the Andes centered on Lake Titicaca, **(b1-3)** Lake Victoria, **(c1-3)** Delta of Mekong with the Tonle Sap, and **(d1-3)** Lake Chad and a portion of Sahel. The same datasets are used than in Figure 7

552 to continuous flooding or wet conditions in the paddy fields (Kuenzer et al., 2013). Thirdly, in Lake Victoria and
 553 Lake Titicaca, a spatial heterogeneity is observed with higher reflectivity (associated to C3 and C4) observed
 554 closer to the banks. This is attributed to the effect of the winds on large lakes and was previously reported in
 555 the literature, especially over Lake Victoria (Al-Khaldi et al., 2021b). The roughness of water surfaces due to the
 556 wind waves can nullify the coherent scattering assumption, and lead to a decrease of surface reflectivity (Chew
 557 & Small, 2020).

558 The CYGNSS reflectivity also depends on the dominant type of land cover inside a pixel. Figure 9 presents
 559 the distribution of CYGNSS clusters into the aggregated LC classes defined in Table 1, either as the total number
 560 of pixels (Figure 9.a) or the percentage (Figure 9.b) in each class. Only pixels with a dominant type of LC covering
 561 at least 80% of the pixel are considered to avoid an influence of LC mixing. First, we notice a strong dominance at
 562 the global scale of non-flooded LC types (bare soils, dry shrubs and herbaceous, non-flooded forests, croplands
 563 non irrigated), with fewer pixels affected by permanent or seasonal water. These dry classes are composed
 564 quasi-exclusively of the CYGNSS clusters C1 and C2, with the lowest reflectivity values, and include also a part
 565 of C3, with high seasonal variations of $\Gamma_{90\%}$ and other CYGNSS-derived parameters. Then, we make several
 566 assessments over flooded areas. The flooded forests are mostly composed of C1 and C2, while the flooded shrubs
 567 and herbaceous are mainly composed of C3 and C4, with higher $\Gamma_{90\%}$ and $\Gamma_{90\%-50\%}$ values and seasonality
 568 (Figure 6). In densely forested areas, the L-band reflected signals recorded by CYGNSS can be either strongly
 569 attenuated on their way to or from the reflecting surface, or scattered by the top of the canopy. In both cases, the
 570 ability of CYGNSS to detect inundations below the canopy is affected. The irrigated croplands, mainly located

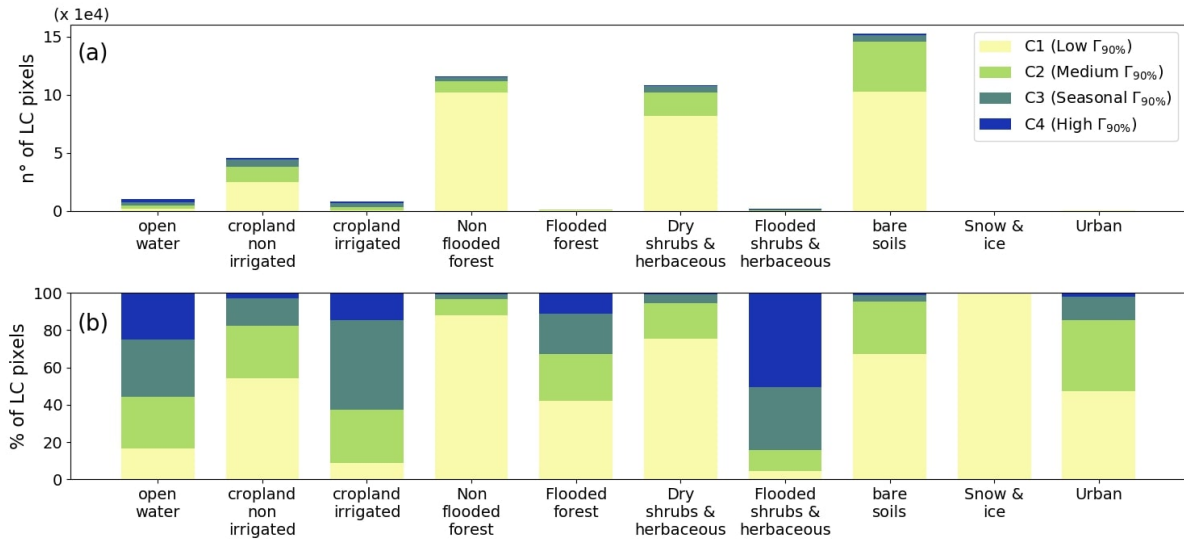


Figure 9: Repartition of the CYGNSS clusters into the main Land Cover types (see Table 1 for the aggregation of CCI LC classes). (a) Number of pixels from each cluster, (b) Percentage of pixels from each cluster.

571 in the paddy fields in Southeast Asia, are dominated by the pixels with a strong seasonal signal in C3. On the
 572 other hand, the croplands non-irrigated are dominated by the dry pixels in C1. Both also contribute in the
 573 cluster C2, highlighting a mixing between these two classes and some misclassifications in Table 5. Non-flooded
 574 croplands and herbaceous covers affected by large seasonal rainfall present high SM values, responsible for a
 575 high CYGNSS reflectivity. Finally, open water bodies are divided between low and high reflectivity clusters. This
 576 should be linked to: i) the attenuation or scattering of the signals in equatorial forests and the non-detection of
 577 small streams, and ii) lower returned signal power on large windy lakes as shown in Figure 8.

578 4.3. Comparison against flood products at regional and global scales

579 In this subsection, we analyze the correlations between CYGNSS-derived parameters and flood reference
 580 products. Because the spatial resolution of GIEMS is 0.25° , CYGNSS has also been gridded and clustered into
 581 an equivalent 0.25° grid for further analysis. We only present the results for Γ_{median} which show the best cor-
 582 relations, as $\Gamma_{90\%}$ is sometimes saturated with a fraction of water inside the pixel. The relationship between
 583 CYGNSS reflectivity and the fraction of water in the footprint is not linear (Chew & Small, 2020). Thus, we
 584 evaluated both Pearson's linear and Spearman's rank correlations. The latter evaluates whether the two vari-
 585 ables are linked with a monotonic function, and should perform better for non-linear relationships. In fact, the
 586 results are slightly better using Spearman's R, in particular for the regional comparisons against MODIS dataset
 587 (Section 4.3.2). Spearman's temporal correlations between Γ_{median} and the dynamic inundation maps at global
 588 and regional scales are therefore presented in Section 4.3.1 and Section 4.3.2, and in Figure 10-11. Finally, the
 589 spatial correlations against RFWs static inundation maps are presented in Section 4.3.3.

590 4.3.1. Global comparison of CYGNSS and GIEMS

591 Figure 10 presents the Spearman's correlation coefficients in every pixel between CYGNSS Γ_{median} and
592 GIEMS Surface Water Extent (SWE) at 0.25° (Figure 10.a). A strong correlation ($R > 0.8$) is obtained in most of
593 the major floodplains located in CYGNSS's spatial coverage, where the seasonality drives both signals due to the
594 high temporal variations of SWE. It is the case in Southeast Asia and India, characterized by the annual monsoon
595 events and irrigated paddy fields in the Ganges-Brahmaputra, Irrawaddy, Mekong and Yangtze basins. In South
596 America also, the seasonal rainfalls cause large floods in Llanos de Orinoco, in the Amazon basin (including
597 Llanos de Mojos and the Branco River), or in La Plata basin (including the Pantanal wetlands). On the contrary,
598 poor results are obtained along some of the Amazon and Congo tributaries, in the upstream parts of these basins.
599 This can be attributed to either the vegetation effect on Γ_{median} , or to a lower seasonality in both signals due to a
600 continuous, high SWE, leading mechanically to a lower correlation. Low or even sometimes negative correlations
601 are also observed in some coastal areas. The surface water estimations from GIEMS can be contaminated by
602 the ocean contribution, although it is expected to be filtered out. Finally, negative correlations are also observed
603 over some land areas (Figure 10). We had a closer look at two specific targets in East Asia. These regions mostly
604 comprise non irrigated croplands and herbaceous land cover, and they showed both a seasonal SWE cycle with
605 low amplitude in GIEMS, and a low signal in CYGNSS with episodic variations. GIEMS likely overestimates
606 SWE in these areas during the wet season, while CYGNSS peaks may be a response to SM or short duration
607 floods following intense precipitation.

608 Figure 10.b presents the average of CYGNSS vs. GIEMS Spearman correlations over the same river basins
609 than in Figure 6, for C3, C4 and all CYGNSS clusters. Cluster C3 in orange and C4 in red show an average
610 correlation over 0.6 for most of the basins. The results in the Orinoco, Ganges, Niger, Lake Chad, Amazon and
611 Parana basins are globally consistent because the water cycle is driven by seasonal floods and irrigation. Two
612 main exceptions are the Congo and Mekong basins where the seasonal variations of reflectivity are very weak
613 (below 0.1). The low correlations observed can be due to either a constant or random signal in both GIEMS
614 and CYGNSS observables. In the Congo basin, the vegetation attenuates CYGNSS signals and provokes a lower
615 detection of inundations below the canopy, and alternating rainfalls in the northern and southern hemispheres
616 produce bimodal variations of inundation extent. In the Mekong basin, a continuous flooding or irrigation
617 in paddy fields, including several parts of the Delta of Mekong (Kuenzer et al., 2013), certainly reduces the
618 seasonality of the signals.

619 4.3.2. Regional comparison

620 The comparison with GIEMS SWE gives an indication of the correlation between CYGNSS reflectivity and
621 flood dynamics at the global scale, but at the regional scale GIEMS is less adequate. First, it is gridded at 0.25° of
622 spatial resolution, thus the information can be degraded when compared to CYGNSS 0.1° grid. Also, we gridded
623 CYGNSS into at 0.25° for comparing against GIEMS, which is not the optimal spatial resolution of this product.
624 Moreover, CYGNSS at 0.1° provides information about the flood dynamics up to a 7-day temporal resolution, and

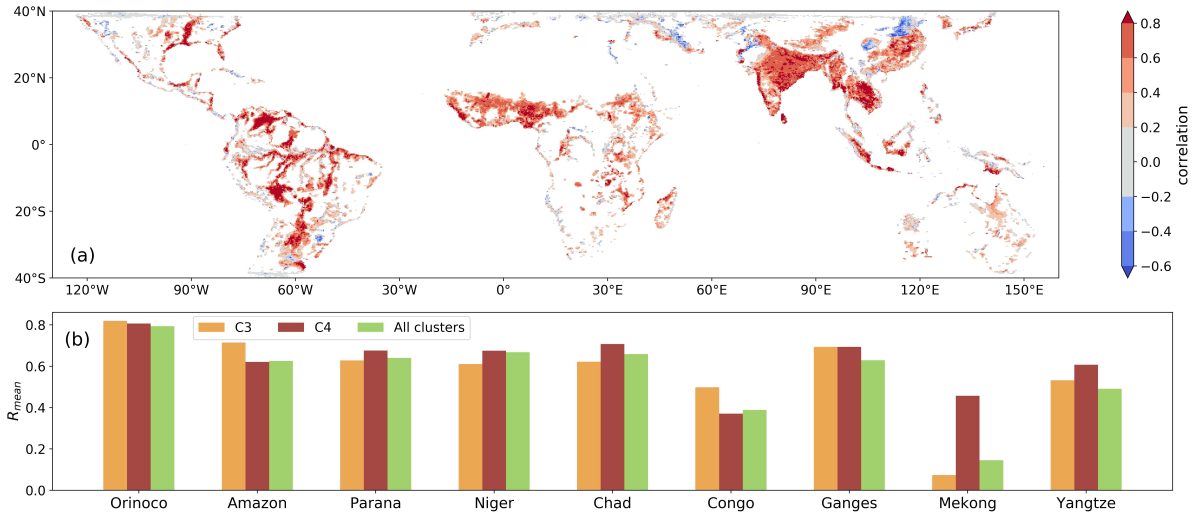


Figure 10: Spearman correlations between CYGNSS Γ_{median} at 0.25° spatial resolution and GIEMS-2 from August 2018 to July 2019. (a) Map of correlations over the flooded areas in GIEMS (maximal SWE > 20%), (b) Barplot of average correlations for CYGNSS clusters C3, C4 and all clusters in 9 river basins.

625 up to a daily time-scale at 0.25°, while GIEMS has a monthly time sampling. It also has uncertainties, especially
 626 in densely forested regions, where it is unclear whether flood signatures can be fully identified in the brightness
 627 temperatures at K-band from SSM/I. Finally, the large estimations of seasonal SWE in GIEMS, particularly in
 628 the Sahel region and the Indian subcontinent, may be overestimated due to the confusion between standing
 629 water and saturated soils during rainfall periods. For all these reasons, we also performed a regional comparison
 630 between CYGNSS Γ_{median} and the SWE derived from MODIS-based regional dynamic flood maps at 500 m
 631 spatial and 8-day temporal resolutions (see Section 2.2).

632 Figure 11 presents the results of this comparison over 3 regions: La Plata basin including the Parana, Uruguay
 633 and Paraguay rivers (Figure 11.a1-2), the Inner Niger Delta (IND) (Figure 11.b1-2), and the Lower Mekong Basin
 634 (LMB) including Tonle Sap and the Delta of Mekong (Figure 11.c1-2). Table 2 show that these regions have
 635 experienced above-average water level peaks during the study period, which are usually correlated with larger
 636 inundated areas. For every region, both maps of maximum flooded extent (as the percentage of water inside the
 637 pixel) and Spearman's correlation coefficients between the time series of SWE and Γ_{median} are shown. Only
 638 the correlations on pixels with a maximum flooded extent above 20% are presented. Over La Plata basin, we
 639 obtain medium ($R > 0.4$) to high ($R > 0.8$) values in the major flooded areas along the streams of the Parana and
 640 Paraguay rivers. In particular, the correlations are high in the Pantanal wetlands ($\sim 58^\circ\text{W}, 20^\circ\text{S}$), in the Paraguay
 641 River and its confluence with the Parana River, and in wetlands close the Salado River in the region of Santa Fé
 642 ($\sim 61^\circ\text{W}, 29^\circ\text{S}$). The values are lower ($R \sim 0.5$) in the major part of the Parana flooded savannas. This could be
 643 due to continuous high reflectivity in this region affected by permanent floods or very high SM content. Low
 644 correlation values are obtained along the streams of the Uruguay and the upper Parana rivers, as well as in
 645 mountainous regions along the Andes.

646 The correlations over the LMB are heterogeneous, with high values over the floodplains and irrigated crop-

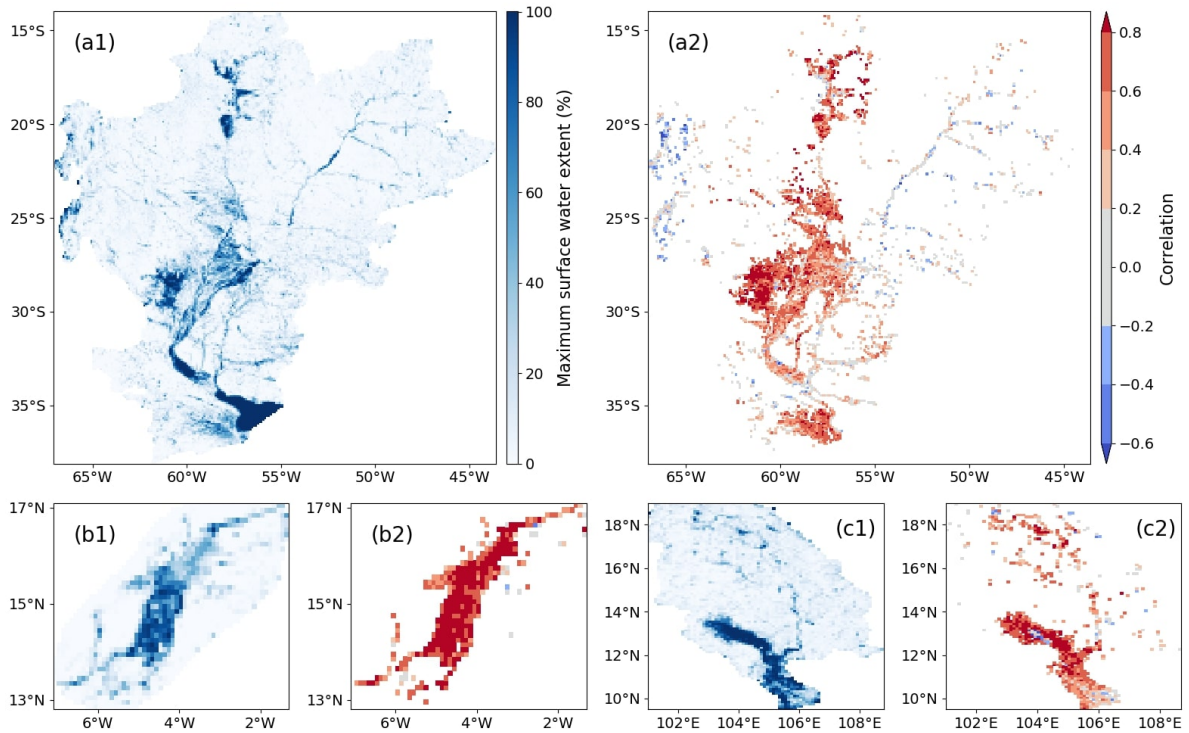


Figure 11: Correlation between CYGNSS Γ_{median} and SWE derived from MODIS over 3 flooded regions. (a1-2) show the maximum water extent in the year and the pixel-by-pixel correlations between water extent and Γ_{median} over La Plata basin, (b1-2) are the equivalent plots over the Inner Niger Delta (IND), and (c1-2) are the equivalent plots over the southern Mekong basin (including the Delta of Mekong and Tonle Sap).

647 lands near the Tonle Sap and along the stream of the Mekong River. On the contrary, low and even negative
 648 correlations are obtained over the Tonle Sap itself, in some parts of the Delta and in isolated pixels. Figure 12
 649 present the time series of SWE and Γ_{median} in 4 neighboring pixels located near the Tonle Sap. The two left
 650 panel pixels (Figure 12.a and Figure 12.c) show a very high seasonality for both parameters, with a water extent
 651 varying from 0 to 100% during the year. It likely corresponds to seasonal floodplains, and the correlations calcu-
 652 lated between the time series are around 0.9. On the contrary, the pixels plotted in Figure 12.b and Figure 12.d
 653 show limited variations in water extent throughout the year, with values systematically over 90% and 50%, re-
 654 spectively. They are mainly covered by permanent water from Tonle Sap. There, the variations of Γ_{median} are
 655 not correlated with variations in the inundation extent. Moreover, in all the pixels, we observe high fluctuations
 656 of Γ_{median} with an amplitude reaching ~ 0.4 and a period of one to several months. These fluctuations mostly
 657 occur when a large fraction of water is present inside the pixel. It could be linked to variations of water rough-
 658 ness over Tonle Sap, the greatest lake in southeast Asia. Moreover, similar time series of Γ_{median} with high
 659 amplitude fluctuations were found to be located close to the banks of Lake Victoria, where the direction and
 660 speed of winds can cause an alternation between coherent and incoherent scattering regimes. Unfortunately,
 661 we were not able to find wind speed data close enough to Tonle Sap to compare with Γ_{median} time series. The
 662 understanding of this phenomena could help further work on retrieving SWE using CYGNSS reflectivity or co-
 663 herency. Other pixels in the Delta of Mekong show low correlation values, but large parts of this area are flooded
 664 or wet throughout the year (Kuenzer et al., 2013).

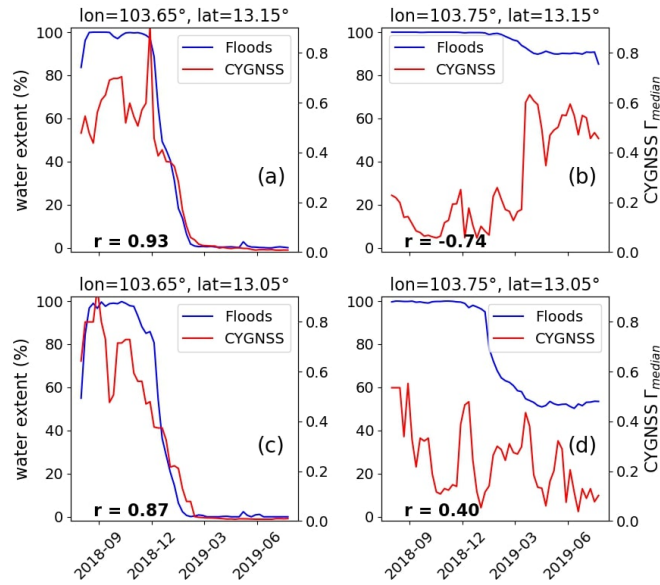


Figure 12: Time series of CYGNSS Γ_{median} (in red) and SWE from MODIS (in blue) with their correlation, for four pixels near the Tonle Sap in the Mekong basin.

665 Finally, the results over the IND show a very good consistency between the time series of SWE and Γ_{median} .
 666 The correlations are greater than 0.8 in most of the pixels. It indicates a strong correspondence between the
 667 dynamics of floods and CYGNSS reflectivity in this region. It is certainly due to two reasons: i) the low vegetation
 668 cover cause lower uncertainties in both CYGNSS observations and the reference inundation maps, and ii) a strong
 669 seasonality is observed in the precipitation and flooding events, so Γ_{median} is low during the dry season unlike
 670 other floodplains in the LMB and the Parana.

671 4.3.3. Spatial correlations at the regional scale

672 Spatial correlation coefficients were also calculated between Γ_{median} and the SWE derived from static RFWs
 673 maps (Tootchi et al., 2019), at the time of the maximum flooded extent during the year. They are estimated for the
 674 9 river basins presented in Figure 6 and Figure 10, and values are reported in Table 6. The spatial correlations in
 675 the Orinoco, Amazon, Parana, Ganges-Brahmaputra and Yangtze basins are high, ranging between 0.74 and 0.77,
 676 showing a good correspondence between the reference maps and CYGNSS reflectivity at the flood maximum
 677 extent. On the contrary, spatial correlations are lower in the other basins and especially in the Sahel region (0.52
 678 for Niger, 0.51 for Lake Chad). This highlights the contribution of multiple factors in the scattering of GNSS
 679 signals over these areas, and maybe uncertainties in the RFWs dataset. While the temporal correlations indicate
 680 whether the variations of SWE are linked with an increase in CYGNSS reflectivity, the spatial correlations are
 681 particularly sensitive to a saturation of both the reference and CYGNSS signals during the wet season. High SM
 682 can provoke high CYGNSS reflectivity, and also an overestimation of the fraction of water estimated in GIEMS,
 683 whose uncertainty is further propagated in the RFWs dataset (see Section 2.2.1 for more details).

Table 6: Spatial correlations between CYGNSS Γ_{median} and the percentage of water derived from RFWs static inundation maps (Tootchi et al., 2019), in 9 river basins inside the area of coverage. The values of Γ_{median} are extracted at the time of the maximum flooded extent.

River basin	Orinoco	Amazon	Parana	Niger	Chad	Congo	Ganges	Mekong	Yangtze
Spatial R	0.76	0.77	0.75	0.52	0.51	0.58	0.75	0.66	0.74

684 5. Discussion

685 The objective of this study was to assess the potential of CYGNSS reflectivity for a pan-tropical mapping
686 of flood dynamics. Based on the results presented in Section 4, we discuss several points to pave the way to a
687 CYGNSS-based inundation product. To begin with, we take a broader view on the interests and limitations of our
688 methodology, as well as the uncertainties in the reference datasets considered. We then discuss the attenuation
689 of GNSS-R signals by the vegetation, especially over tropical forests, and the feasibility of flood detection under
690 dense canopies using CYGNSS reflectivity. We also point out the misleading role of high forward scattering in
691 the specular direction in arid areas, due to changes in morphology, *i.e.* roughness for CYGNSS, but also lithology
692 (sand vs. rock, see Section 5.4).

693 5.1. Results of the K-means Clustering

694 We have used the K-means clustering algorithm with a Dynamic Time Warping similarity measure to per-
695 form the clustering of CYGNSS reflectivity time series. Other common unsupervised classification algorithms
696 were tested such as Agglomerative Clustering or Birch, but the best results were obtained with K-means. The
697 implementation of a DTW similarity measure instead of a simple Euclidean distance makes it more robust to
698 shifts in phase and distortion in time between time series of reflectivity. Promising results were obtained and
699 analyzed in this study, but the empirical approach led us to discuss our choices in the implementation of the
700 methodology.

701 First, the optimal number of clusters needed to be determined. We were not able to calculate any criteria
702 like the Calinski-Harabasz and the Silhouette scores with the implementation of the DTW similarity measure.
703 We also tested our methodology with a common Euclidean distance in the K-means approach, which gave us an
704 optimal number of 2 clusters with both the Calinski-Harabasz and the Silhouette scores. This is a highly simpli-
705 fied version of the phenomena as dry land vs. flooded areas, and does not give information on the seasonality
706 of floodplains. Thus, we empirically determined the optimal number of clusters, which was found to be $k = 4$
707 (Figure 6 and Table 5). The two clusters with highest reflectivity are mostly associated to the occurrence of water,
708 one with permanent or long-lasting floods, the second with high seasonal variations. A third cluster is composed
709 of a mix of wetlands and bare soils with medium reflectivity, and can be especially sensitive to an increase of
710 CYGNSS reflectivity over non-flooded areas due to high SM content. The last cluster is mainly associated to dry
711 soils, never flooded throughout the year. We also tried the clustering with several combinations of parameters
712 from Figure 4: 1) Γ_{mean} only, 2) Γ_{median} only, 3) $\Gamma_{90\%}$ only, 4) $\Gamma_{90\%-50\%}$ only, 5) Γ_{median} and $\Gamma_{90\%}$, 6) Γ_{mean}
713 and Γ_{std} , 7) Γ_{mean} , Γ_{std} , $\Gamma_{90\%}$ and Γ_{median} . All the confusion matrices and the plots (similar to Table 5 and

714 Figure 6, respectively) were evaluated for each version of the clustering, leading to the determination of the best
715 scenario.

716 To ensure the stability of our clustering, we performed a sensitivity analysis on 30 iterations of the K-means++
717 / DTW clustering. It was shown that the 30 results are quite stables, especially in terms of inertia (see Table 3).
718 However, the random (although weighted) choice of the initial 4 centroids by the K-means++ algorithm leads
719 to differences in the final results. In 25 results out of 30, very small differences are observed in the output
720 labels, especially for clusters C3 and C4 associated to water bodies (see Figure 6). The last 5 versions show
721 lower agreement with each-other. The correspondence (*i.e.* percentage of pixels similarly labelled between two
722 versions of the clustering) has a minimum of 80.26%, and a median of 94.64% (Table 3). As a consequence, we
723 adapted our methodology to guarantee the reproducibility of the clustering. The mean time series of cluster
724 centers C1 to C4 were computed from the 30 random DTW outputs, and selected as user-defined centroids for
725 a new K-means / DTW clustering. This final version was analyzed in Section 4.

726 Finally, the DTW was implemented to manage shifts in time between the flooding events in different regions
727 of the world. However, it has a limitation due to the boundary condition. The DTW algorithm starts with the
728 first index and finishes with the last index of each time series that are compared. As a consequence, the values
729 of $\Gamma_{90\%-50\%}$ and other CYGNSS parameters at the boundaries of the time series play a determinant role for the
730 clustering. We use only one year of CYGNSS observations because of the high computational capacities required
731 to process and analyze this dataset, and due to the experimental nature of our methodology whose interest
732 needed to be proven before a global application to the 5-year CYGNSS dataset. To avoid the boundary effect,
733 we implemented a padding of the 1-year time series of our parameters to create artificially a 3-year dataset. The
734 results prove that this technique does not affect the ability of the K-means / DTW clustering to extract a seasonal
735 flood signal from both the wetlands in the northern (*e.g.* Orinoco, Rio Branco, Ganges, Yangtze, Mekong) and
736 southern (*e.g.* Llanos de Mojos, Pantanal, Parana) hemispheres.

737 5.2. Reference inundation maps

738 The reference datasets used in this study are also sources of uncertainties. The static inundation maps from
739 Tootchi et al. (2019) were used as a delineation of permanent water bodies and regularly flooded areas. We first
740 tried to use the composite wetlands (CWs) maps as it contains both the regularly flooded wetlands (RFWs) and
741 the groundwater-driven wetlands (GDWs). It seemed logical to us that GDWs also play a role in the scattering of
742 GNSS signals, as they are an important source of SM in saturated soils. However, we noticed a strong saturation
743 of the CWs maps in several river basins. As an example, the entire Amazon basin and a great part of Sahel were
744 listed as partially or totally affected by floods, which is largely exaggerated. Also, spatial correlation coefficients
745 calculated with CYGNSS Γ_{median} show higher values with RFWs maps both at the global and regional scales.
746 For the Amazon basin, the spatial correlation is 0.77 between Γ_{mean} and the SWE from RFWs maps (Table 6),
747 and is 0.48 with CWs maps. As a consequence, we decided to use the RFWs maps for comparison with CYGNSS
748 datasets. Additionally, the thresholding of RFWs variables into the 5 reference classes defined in (Table 4) is

749 debatable. The open water class (A) corresponds to pixels covered with, at least, 10% of open water. When
750 plotting Γ_{mean} as a function of open water extent, the Γ_{mean} values are saturated above this threshold. On the
751 contrary, the function of Γ_{mean} vs. inundation extent is linear, with no saturation of the signal when increasing
752 the fraction of flooded areas in the pixel. The separation of reference classes B, C and D is then arbitrary, with
753 thresholds corresponding to high, medium or low inundation extent in the pixel.

754 The uncertainties of GIEMS are mainly associated to its low spatial resolution (0.25°), leading to a low sen-
755 sitivity to small water bodies. It is also influenced by dense vegetation covers, and high seasonal SM content
756 confounded with surface water in several regions (Sahel, Indian subcontinent). These are sources of uncertainty
757 for our analysis because even Tootchi's RFWs dataset is based on GIEMS-D15 (Fluet-Chouinard et al., 2015),
758 derived from GIEMS itself. Still, the comparison of CYGNSS vs. GIEMS and MODIS estimated SWE looks con-
759 sistent at the regional scale, although the spatial resolutions are different (0.25° for the first, 0.1° for the latter).

760 5.3. Reflectivity over vegetated areas

761 The detection of floods under equatorial forests remains difficult even with the use of microwave signals. It is
762 a limitation of GIEMS (Prigent et al., 2020) for example. The use of CYGNSS data is promising because: i) L-band
763 GNSS signals penetrate deeper the canopy than shorter wavelengths/higher frequencies in the microwave do-
764 main, ii) it provides information at a higher spatiotemporal resolution than the passive microwave sensors. Sev-
765 eral studies took advantage of these characteristics. Rodriguez-Alvarez et al. (2019) classified CYGNSS corrected
766 Signal-to-Noise Ratio (SNR) as flooded vegetation (FV), open water and dry land. This study was performed in a
767 small subset of the Amazon basin and showed a detection of FV around 70%. Then, Carreno-Luengo et al. (2020)
768 studied the relationship between CYGNSS observables, including the reflectivity Γ , and AGB over subsets of
769 the Congo and Amazon basins. A polynomial fit was used to characterize the vegetation attenuation at several
770 incidence angles, and to further derive CYGNSS-based maps of AGB over equatorial forests. These maps were
771 consistent with reference datasets up to ~ 350 Mg/ha. Also, Li et al. (2021) derived the coherency of Beidou-3
772 raw IF tracks over flooded areas along the Mississippi River, in densely vegetated areas. High coherency, which
773 is linked to the presence of water below the canopy, was obtained for AGB up to 200-300 Mg/ha. And finally, the
774 PR defined in Al-Khaldi et al. (2021a,b) as a coherency proxy has shown low sensitivity to vegetation, allowing
775 the detection of small river streams obscured by trees.

776 In Figure 6.a and Figure 7, the streams of the Congo and Amazon rivers and their tributaries are well de-
777 lined. We can still question whether CYGNSS is able to monitor nearby floodplains under vegetation cover.
778 Figure 13 presents the distribution of AGB in CYGNSS clusters C1 to C4, for both flooded and non-flooded
779 pixels. All pixels with an occurrence of water greater than 0% in the 0.1° regrided RFWs dataset are considered
780 as flooded, which likely overestimates the inundated areas. Only pixels in South America are considered in this
781 figure, to obtain a balance between flooded and dry pixels, and between high and low AGB values. The dynamic
782 range of AGB is approximately 0-300 Mg/ha and shows two peaks for all clusters. The first one, between 0 and
783 50 Mg/ha, corresponds both to dry pixels with few vegetation, and to large floodplains with herbaceous-type

784 land cover, as in the Llanos de Orinoco, Llanos de Mojos, and the Pantanal wetlands (see Figure 7 for dominant
785 land cover types in South America). The second one, between 200 and 300 Mg/ha, corresponds to dense forests
786 mainly located in the Amazon basin. These forests are either dry (cluster C1), wet or flooded (clusters C2 to C4).
787 In particular, flooded pixels in C3 and C4 mostly represent the large floodplains and open water (see Figure 6,
788 Figure 7 and Table 5), with low AGB. However, the fourth decile (*i.e.* the top 25% of AGB values) in flooded pixels
789 from C3 and C4 ranges from ~ 150 Mg/ha to ~ 300 Mg/ha. The results in Figure 13 show that the K-means /
790 DTW clustering based on CYGNSS reflectivity is able to detect either flooded areas below the canopy or narrow
791 river streams surrounded by vegetation, in pixels with dense forests and average AGB as high as 250-300 Mg/ha.
792 Some sources of uncertainties can be related to: i) signals from wet, saturated soils without standing water, ii)
793 errors in the definition of flooded areas using RFWs dataset, and iii) the attenuation of GNSS-R signals by the
794 vegetation, especially at high incidence angle, leading to a potential extinction of the coherent component on
795 which we base our analysis (Al-Khaldi et al., 2021a; Loria et al., 2020). The results presented in Figure 9 show a
796 lower detection of the inundations under forest land cover types, when compared to an herbaceous cover.

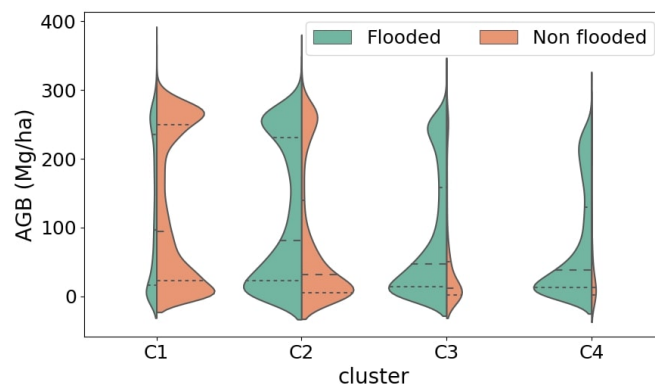


Figure 13: Distribution of the AGB for flooded and non-flooded pixels over South America in the 4 CYGNSS clusters. The dashed lines represent the quartiles of the distributions. Flooded pixels are defined with a fraction of water greater than 0% in the 0.1° regrided RFWs dataset.

797 5.4. Reflectivity over bare soils

798 In Figure 5 and Figure 6.a, we notice the heterogeneity of $\Gamma_{90\%}$, $\Gamma_{90\%-50\%}$ and CYGNSS clusters over arid
799 regions, where bare soils is the dominant land cover type. In particular, reflections over deserts in the Sahara
800 and the Arabica Peninsula have a high dynamic range, with $\Gamma_{90\%}$ values ranging from 0 to ~ 0.4 . As the time
801 series of $\Gamma_{90\%}$ and $\Gamma_{90\%-50\%}$ are almost constant in the year due to a very low moisture, these areas can be
802 interpreted as open water bodies, in particular when the reflected signals over the latter are attenuated as for
803 wind conditions over lakes (see Figure 8). An important forward scattering of GNSS-R signals has already been
804 observed in the literature, and mainly linked to areas of low small-scale roughness. In particular, the water
805 mask given by Al-Khaldi et al. (2021a) also had false alarms over desert regions characterized by (almost) flat
806 surfaces, based on their PR coherency metric. They handled the problem with a filtering of the locations showing
807 a recurrent coherence, and a 0% occurrence of water in the mask from Pekel et al. (2016). This type of filtering

808 could be easily applied to our reflectivity dataset, and is a requirement for a further inversion of a fractional
809 water extent product.

810 The state of the art beyond the scope of CYGNSS-related studies shows that anomalies in the radar signals
811 over arid regions are well known for several active and passive sensors, and can be related to the geological
812 and lithologic properties. Prigent et al. (2015) analyzed the multiangle backscattering at Ku-band from Tropical
813 Rainfall Measurement Mission / Precipitation Radar (TRMM / PR) and QuikSCAT in the inter-tropical zone
814 covered by CYGNSS. They showed that sand dunes have lower backscattering coefficients when compared to
815 rock deserts, because of an important volume scattering in dry sand and a relatively low large-scale roughness.
816 Similar effects were also observed at C-band using ASCAT (Favras et al., 2015). This phenomenon increases with
817 an increasing incidence angle. Similarly, the microwave emissivities over arid regions show higher values for
818 sand dunes due to the contribution of both the surface and deeper soils to microwave emissions (Jiménez et al.,
819 2010). GNSS-R forward scattering is likely subjected to the same phenomena, as the spatial agreement between
820 $\Gamma_{90\%}$ and $\Gamma_{90\%-50\%}$ maps and TRMM / PR-based maps of backscattering coefficients in Prigent et al. (2015) is
821 good.

822 5.5. Guidelines for a CYGNSS-based dynamic product of SWE

823 This study shows that both permanent water and seasonal floodplains can be monitored using CYGNSS
824 reflectivity. In particular, the 0.1° spatial resolution and 7-day temporal resolution grid merges by time and loca-
825 tion the bistatic observations, and offers the possibility to compute time series of several statistical parameters
826 (see Section 3). In particular, $\Gamma_{90\%}$ is very sensitive to the presence of a fraction of water, and $\Gamma_{90\%-50\%}$ can be
827 used to extract pixels with recurrence or occurrence of water. Also, the comparison of Γ_{mean} with the fraction
828 of water in the pixel, either from static or dynamic estimations, shows an interesting linear trend. This linearity
829 could be further exploited to produce a CYGNSS-based SWE product, covering the pan-tropical area.

830 For this, the confounding effects of several geophysical parameters need to be removed. False alarms over
831 deserts can be avoided with a simple filtering as in Al-Khalidi et al. (2021a). Then, a correction of reflectivity
832 for the vegetation attenuation must be implemented, which is usually performed using the incidence angle and
833 ancillary L-band Vegetation Optical Depth (L-VOD) data provided by radiometers such as SMOS (Wigneron
834 et al., 2021) or SMAP (Konings et al., 2017; Li et al., 2022b). Also, GIEMS-2 (Prigent et al., 2020), assumes the
835 linearity of SWE retrieval under given vegetation conditions, and the dataset is therefore binned depending on
836 the values of vegetation parameters. Based on this idea, CYGNSS dataset could be binned with either NDVI,
837 AGB or VOD to improve the linearity of Γ_{mean} vs. SWE relations. The effect of small-scale and large scale
838 roughness on the performances of future SWE product could be important to study. Water roughness over large
839 lakes is a limitation due to a dominant incoherent scattering regime, so it must also be taken in account. As we
840 focus on dynamic estimations of SWE in floodplains, recurrent open water bodies could be filtered out as they
841 are well delineated using other remote sensing sensors. Finally, the confounding effect of SM can lead to an
842 overestimation of flooded areas in regions affected by large seasonal rainfall. Further investigations could use

843 the coherence proxy defined in Al-Khaldi et al. (2021a,b), in helping to filter out the pixels with strong reflectivity
844 that is associated to very wet soils with no surface water.

845 6. Conclusion

846 We have analyzed CYGNSS land surface reflectivity to evaluate its potential for a global mapping of flood
847 dynamics. A 0.1° spatial resolution and weekly time sampling of CYGNSS reflectivity was found to be the
848 most suitable compromise between high spatial and temporal resolutions. We have used a K-means clustering
849 technique with DTW similarity measure to separate: i) the low, constant reflectivity signals from dry land, ii)
850 the high signals from open water and long-lasting inundations, and iii) the seasonal signals associated to large
851 floodplains. Static and dynamic inundation maps along with other ancillary datasets were used to analyze the
852 clustering results. The largest water bodies, floodplains and irrigated croplands areas are detected. Various
853 sources of misclassification are identified. The flooded areas are mostly detected in absence of vegetation or
854 under herbaceous cover, but less accurately under forests. The concordance between CYGNSS parameters and
855 the static inundation maps is not good in the Cuvette Centrale of Congo in particular. The detection of water
856 bodies is also weakened under windy conditions over large lakes, as it was already reported by several studies.
857 In the deserts, a low reflectivity is observed on sand dunes where the penetration of microwave signals is high,
858 and a high reflectivity is observed on flat, rocky regions where a specular scattering was found to create false
859 alarms. However, CYGNSS clusters and parameters make possible to identify the main floodplains and open
860 water areas, including samples in areas with AGB as high as ~ 300 Mg/ha along the streams of Amazon and
861 Congo rivers. The spatial correlations between Γ_{median} and static inundation maps were calculated at the time
862 of the maximum SWE. They show high values (R ranging from 0.74 to 0.77) in 5 large river basins and lower
863 values in Congo, Lake Chad and Niger, highlighting the contribution of multiple known factors (vegetation,
864 soil moisture, small and large scales roughness, type of soil, SWE) in the GNSS-R forward-scattered signals.
865 Temporal correlations were also calculated between Γ_{median} and SWE from either GIEMS or regional MODIS-
866 based inundation maps. Regional comparisons over the IND, Parana and Mekong basins perform well and are
867 consistent with global comparison using GIEMS. High values (R > 0.8) are obtained on the principal floodplains
868 in the CYGNSS coverage, with once again the exception of the Cuvette Centrale of Congo. Lower correlations
869 are obtained in the Amazon and Congo tributaries, either due to an attenuation of GNSS-R signals by vegetation
870 canopies, or to the uncertainties of reference datasets in these areas.

871 Finally, our results show that a global mapping of inundation dynamics using CYGNSS reflectivity is possible,
872 as some open water and flood patterns were clearly identified in the K-means / DTW clustering results. We tried
873 to list the several sources of misclassification to identify contributing factors in CYGNSS reflectivity either at
874 the global or regional scale. We look forward to producing a dynamic mapping of floods using CYGNSS, with
875 ancillary and reference datasets helping to characterize the relation between CYGNSS reflectivity and SWE.

876 **Acknowledgements**

877 P. Zeiger is funded by a PhD grant from Ministère de l'Enseignement Supérieur, de la Recherche et de
878 l'Innovation (MESRI). This work was supported by Centre National de la Recherche Scientifique (CNRS) and
879 Centre National d'Etudes Spatiales (CNES) through INSU PNTS grant URGENS and TOSCA grants SWHYM
880 and SCOMAG, respectively.

881 We thank all the reviewers for their helpful and detailed suggestions, to help us improve the revised version
882 of this manuscript.

883 **References**

- 884 Acreman, M., & Holden, J. (2013). How Wetlands Affect Floods. *Wetlands*, 33, 773–786. doi:10.1007/
885 s13157-013-0473-2.
- 886 Al-Khaldi, M. M., Johnson, J. T., Gleason, S., Chew, C. C., Gerlein-Safdi, C., Shah, R., & Zuffada, C. (2021a). Inland
887 water body mapping using cygnss coherence detection. *IEEE Transactions on Geoscience and Remote Sensing*,
888 59, 7385–7394. doi:10.1109/TGRS.2020.3047075.
- 889 Al-Khaldi, M. M., Johnson, J. T., Gleason, S., Loria, E., O'Brien, A. J., & Yi, Y. (2021b). An algorithm for detecting
890 coherence in cyclone global navigation satellite system mission level-1 delay-doppler maps. *IEEE Transactions*
891 *on Geoscience and Remote Sensing*, 59, 4454–4463. doi:10.1109/TGRS.2020.3009784.
- 892 Al-Khaldi, M. M., Johnson, J. T., O'Brien, A. J., Balenzano, A., & Mattia, F. (2019). Time-Series Retrieval of Soil
893 Moisture Using CYGNSS. *IEEE Trans. Geosci. Remote Sensing*, 57, 10.
- 894 Arthur, D., & Vassilvitskii, S. (2007). k-means++: The Advantages of Careful Seeding. In *Proceedings of the*
895 *Eighteenth Annual ACM-SIAM Symposium on Discrete Algorithms* (pp. 1027–1035). Philadelphia, USA.
- 896 Bartlett, K. B., & Harriss, R. C. (1993). Review and assessment of methane emissions from wetlands. *Chemosphere*,
897 26, 261–320. doi:10.1016/0045-6535(93)90427-7.
- 898 Bergamaschi, P., Frankenberg, C., Meirink, J. F., Krol, M., Dentener, F., Wagner, T., Platt, U., Kaplan, J. O., Körner,
899 S., Heimann, M., Dlugokencky, E. J., & Goede, A. (2007). Satellite cartography of atmospheric methane from
900 SCIAMACHY on board ENVISAT: 2. Evaluation based on inverse model simulations. *J. Geophys. Res.*, 112,
901 D02304. doi:10.1029/2006JD007268.
- 902 Berndt, D. J., & Clifford, J. (1994). Using Dynamic Time Warping to Find Patterns in Time Series. In *AAAI-94*
903 *Workshop on Knowledge Discovery in Databases* (pp. 359–370). volume 10.
- 904 Betbeder, J., Gond, V., Frappart, F., Baghdadi, N. N., Briant, G., & Bartholome, E. (2014). Mapping of Central
905 Africa Forested Wetlands Using Remote Sensing. *IEEE J. Sel. Top. Appl. Earth Observations Remote Sensing*, 7,
906 531–542. doi:10.1109/JSTARS.2013.2269733.

907 Bloom, A. A., Palmer, P. I., Fraser, A., Reay, D. S., & Frankenberg, C. (2010). Large-Scale Controls of Methanogen-
908 esis Inferred from Methane and Gravity Spaceborne Data. *Science*, 327, 322–325. doi:10 . 1126/science .
909 1175176.

910 Bullock, A., & Acreman, M. (2003). The role of wetlands in the hydrological cycle. *Hydrol. Earth Syst. Sci.*, 7,
911 358–389. doi:10 . 5194/hess-7-358-2003.

912 Calinski, T., & Harabasz, J. (1974). A dendrite method for cluster analysis. *Comm. in Stats. - Theory & Methods*,
913 3, 1–27. doi:10 . 1080/03610927408827101.

914 Camps, A., Park, H., Pablos, M., Foti, G., Gommenginger, C. P., Liu, P. W., & Judge, J. (2016). Sensitivity of
915 GNSS-R Spaceborne Observations to Soil Moisture and Vegetation. *IEEE J. Sel. Top. Appl. Earth Observations*
916 *Remote Sensing*, 9, 4730–4742. doi:10 . 1109/JSTARS . 2016 . 2588467.

917 Cardellach, E., Fabra, F., Nogués-Correig, O., Oliveras, S., Ribó, S., & Rius, A. (2011). GNSS-R ground-based and
918 airborne campaigns for ocean, land, ice, and snow techniques: Application to the GOLD-RTR data sets. *Radio*
919 *Science*, 46, 1–16. doi:10 . 1029/2011RS004683.

920 Carreno-Luengo, H., Luzi, G., & Crosetto, M. (2019). Sensitivity of CyGNSS Bistatic Reflectivity and SMAP Mi-
921 crowave Radiometry Brightness Temperature to Geophysical Parameters over Land Surfaces. *IEEE J. Sel. Top.*
922 *Appl. Earth Observations Remote Sensing*, 12, 107–122. doi:10 . 1109/JSTARS . 2018 . 2856588. Pub-
923 lisher: IEEE.

924 Carreno-Luengo, H., Luzi, G., & Crosetto, M. (2020). Above-ground biomass retrieval over tropical forests: A
925 novel gnss-r approach with cygnss. *Remote Sensing*, 12. doi:10 . 3390/rs12091368.

926 Chapman, B. D., Russo, I. M., Galdi, C., Morris, M., di Bisceglie, M., Zuffada, C., Downs, B., Lavallo, M., Loria, E.,
927 & O'Brien, A. J. (2022). Comparison of sar and cygnss surface water extent metrics. *IEEE Journal of Selected*
928 *Topics in Applied Earth Observations and Remote Sensing*, 15, 3235–3245. doi:10 . 1109/JSTARS . 2022 .
929 3162764.

930 Chen, Y., Huang, C., Ticehurst, C., Merrin, L., & Thew, P. (2013). An Evaluation of MODIS Daily and 8-day
931 Composite Products for Floodplain and Wetland Inundation Mapping. *Wetlands*, 33, 823–835. doi:10 . 1007/
932 s13157-013-0439-4.

933 Chew, C., Reager, J. T., & Small, E. (2018). CYGNSS data map flood inundation during the 2017 Atlantic hurricane
934 season. *Sci Rep*, 8, 9336. doi:10 . 1038/s41598-018-27673-x.

935 Chew, C., Shah, R., Zuffada, C., Hajj, G., Masters, D., & Mannucci, A. J. (2016). Demonstrating soil moisture
936 remote sensing with observations from the UK TechDemoSat-1 satellite mission. *Geophysical Research Letters*,
937 43, 3317–3324. doi:10 . 1002/2016GL068189.

938 Chew, C., & Small, E. (2020). Estimating inundation extent using CYGNSS data: A conceptual modeling study.
939 *Remote Sensing of Environment*, 246, 111869. doi:10.1016/j.rse.2020.111869.

940 Chew, C. C., & Small, E. E. (2018). Soil Moisture Sensing Using Spaceborne GNSS Reflections: Comparison of
941 CYGNSS Reflectivity to SMAP Soil Moisture. *Geophysical Research Letters*, 45, 4049–4057. doi:10.1029/
942 2018GL077905.

943 Choudhury, B. J. (1991). Passive microwave remote sensing contribution to hydrological variables. *Surveys in*
944 *Geophysics*, 12, 63–84.

945 Clarizia, M. P., Pierdicca, N., Costantini, F., & Floury, N. (2019). Analysis of CYGNSS Data for Soil Moisture
946 Retrieval. *IEEE J. Sel. Top. Appl. Earth Observations Remote Sensing*, 12, 9.

947 Clarizia, M. P., & Ruf, C. S. (2016). Wind speed retrieval algorithm for the cyclone global navigation satellite
948 system (cygnss) mission. *IEEE Transactions on Geoscience and Remote Sensing*, 54, 4419–4432. doi:10.1109/
949 TGRS.2016.2541343.

950 Clarizia, M. P., Ruf, C. S., Cipollini, P., & Zuffada, C. (2016). First spaceborne observation of sea surface height
951 using GPS-Reflectometry. *Geophysical Research Letters*, 43, 767–774. doi:10.1002/2015GL066624.

952 Collett, I., Wang, Y., Shah, R., & Morton, Y. J. (2022). Phase coherence of gps signal land reflections and its
953 dependence on surface characteristics. *IEEE Geoscience and Remote Sensing Letters*, 19, 1–5. doi:10.1109/
954 LGRS.2021.3094407.

955 Crétaux, J.-F., Arsen, A., Calmant, S., Kouraev, A., Vuglinski, V., Bergé-Nguyen, M., Gennero, M.-C., Nino, F.,
956 Rio, R. A. D., Cazenave, A., & Maisongrande, P. (2011). SOLS: A lake database to monitor in the Near Real
957 Time water level and storage variations from remote sensing data. *Advances in Space Research*, 47, 1497–1507.
958 doi:https://doi.org/10.1016/j.asr.2011.01.004.

959 CYGNSS (2020). CYGNSS level 1 science data record version 3.0. ver. 3.0. PO.DAAC, CA, USA. URL: https://doi.org/10.5067/CYGNSS-L1X30 accessed: 2021-10-01.

961 Davidson, N. C., Fluet-Chouinard, E., & Finlayson, C. M. (2018). Global extent and distribution of wetlands:
962 trends and issues. *Mar. Freshwater Res.*, 69, 620. doi:10.1071/MF17019.

963 De Roo, R. D., & Ulaby, F. T. (1994). Bistatic specular scattering from rough dielectric surfaces. *IEEE Transactions*
964 *on Antennas and Propagation*, 42, 220–231.

965 Defourny, P., Vancutsem, C., Bicheron, P., Brockmann, C., Nino, F., Schouten, L., & Leroy, M. (2007). GlobCover:
966 A 300M Global Land Cover Product for 2005 Using ENVISAT MERIS Time Series. In *Proceedings of the ISPRS*
967 *Commission VII Symposium Remote Sensing: From Pixels to Processes* (p. 4). Enschede, The Netherlands.

968 Di Gregorio, A. (2016). *Land Cover Classification System - Classification concepts Software version 3*. Technical
969 Report Food and Agriculture Organisation Roma, Italy.

970 Di Vittorio, C. A., & Georgakakos, A. P. (2018). Land cover classification and wetland inundation mapping using
971 MODIS. *Remote Sensing of Environment*, 204, 1–17. doi:10.1016/j.rse.2017.11.001.

972 Egido, A., Paloscia, S., Motte, E., Guerriero, L., Pierdicca, N., Caparrini, M., Santi, E., Fontanelli, G., & Floury, N.
973 (2014). Airborne GNSS-R polarimetric measurements for soil moisture and above-ground biomass estimation.
974 *IEEE J. Sel. Top. Appl. Earth Observations Remote Sensing*, 7, 1522–1532. doi:10.1109/JSTARS.2014.
975 2322854. Publisher: IEEE.

976 Entekhabi, D., Njoku, E. G., O'Neill, P. E., Kellogg, K. H., Crow, W. T., Edelstein, W. N., Entin, J. K., Goodman,
977 S. D., Jackson, T. J., Johnson, J., & al. (2010). The Soil Moisture Active Passive (SMAP) Mission. *Proc. IEEE*, 98,
978 704–716. doi:10.1109/JPROC.2010.2043918.

979 Eroglu, O., Kurum, M., Boyd, D., & Gurbuz, A. C. (2019). High spatio-temporal resolution cygnss soil moisture
980 estimates using artificial neural networks. *Remote Sensing*, 11. doi:10.3390/rs11192272.

981 ESA (2017). Land cover CCI product user guide version 2. tech. rep. (2017). URL: [maps.elie.ucl.ac.be/
982 CCI/viewer/download/ESACCI-LC-Ph2-PUGv2_2.0.pdf](https://maps.elie.ucl.ac.be/CCI/viewer/download/ESACCI-LC-Ph2-PUGv2_2.0.pdf).

983 Fan, Y., Li, H., & Miguez-Macho, G. (2013). Global Patterns of Groundwater Table Depth. *Science*, 339, 940–943.
984 doi:10.1126/science.1229881.

985 Fatras, C., Frappart, F., Mougou, E., Frison, P.-L., Faye, G., Borderies, P., & Jarlan, L. (2015). Spaceborne altimetry
986 and scatterometry backscattering signatures at C- and Ku-bands over West Africa. *Remote Sensing of
987 Environment*, 159, 117–133. doi:10.1016/j.rse.2014.12.005.

988 Fluet-Chouinard, E., Lehner, B., Rebelo, L.-M., Papa, F., & Hamilton, S. K. (2015). Development of a global
989 inundation map at high spatial resolution from topographic downscaling of coarse-scale remote sensing data.
990 *Remote Sensing of Environment*, 158, 348–361. doi:https://doi.org/10.1016/j.rse.2014.10.
991 015.

992 Foti, G., Gommenginger, C., Jales, P., Unwin, M., Shaw, A., Robertson, C., & Roselló, J. (2015). Spaceborne GNSS
993 reflectometry for ocean winds: First results from the UK TechDemoSat-1 mission. *Geophys. Res. Lett.*, 42,
994 5435–5441. doi:10.1002/2015GL064204.

995 Frappart, F., Biancamaria, S., Normandin, C., Blarel, F., Bourrel, L., Aumont, M., Azemar, P., Vu, P.-L., Le Toan, T.,
996 Lubac, B., & Darrozes, J. (2018). Influence of recent climatic events on the surface water storage of the Tonle
997 Sap Lake. *Science of The Total Environment*, 636, 1520–1533. doi:10.1016/j.scitotenv.2018.04.
998 326.

999 Frappart, F., Zeiger, P., Betbeder, J., Gond, V., Bellot, R., Baghdadi, N., Blarel, F., Darrozes, J., Bourrel, L., & Seyler,
1000 F. (2021). Automatic Detection of Inland Water Bodies along Altimetry Tracks for Estimating Surface Water
1001 Storage Variations in the Congo Basin. *Remote Sensing*, *13*, 22.

1002 Gerlein-Safdi, C., Bloom, A. A., Plant, G., Kort, E. A., & Ruf, C. S. (2021). Improving representation of tropical
1003 wetland methane emissions with cygnss inundation maps. *Global Biogeochemical Cycles*, *35*, e2020GB006890.
1004 doi:<https://doi.org/10.1029/2020GB006890>.

1005 Gerlein-Safdi, C., & Ruf, C. S. (2019). A CYGNSS-Based Algorithm for the Detection of Inland Waterbodies.
1006 *Geophysical Research Letters*, *46*, 12065–12072. doi:10.1029/2019GL085134.

1007 Ghasemigoudarzi, P., Huang, W., De Silva, O., Yan, Q., & Power, D. T. (2020). Flash Flood Detection From
1008 CYGNSS Data Using the RUSBoost Algorithm. *IEEE Access*, *8*, 171864–171881. doi:10.1109/ACCESS.
1009 2020.3025302.

1010 Gleason, S., O'Brien, A., Russel, A., Al-Khaldi, M. M., & Johnson, J. T. (2020). Geolocation, calibration and surface
1011 resolution of cygnss gnss-r land observations. *Remote Sensing*, *12*. doi:10.3390/rs12081317.

1012 Gleason, S., Ruf, C. S., O'Brien, A. J., & McKague, D. S. (2019). The CYGNSS Level 1 Calibration Algorithm and
1013 Error Analysis Based on On-Orbit Measurements. *IEEE J. Sel. Top. Appl. Earth Observations Remote Sensing*,
1014 *12*, 37–49. doi:10.1109/JSTARS.2018.2832981.

1015 Hamilton, S. K., Sippel, S. J., & Melack, J. M. (2004). Seasonal inundation patterns in two large savanna floodplains
1016 of South America: the Llanos de Moxos(Bolivia) and the Llanos del Orinoco(Venezuela and Colombia). *Hydrol.*
1017 *Process.*, *18*, 2103–2116. doi:10.1002/hyp.5559.

1018 Hess, L. L., Melack, J. M., Novo, E. M., Barbosa, C. C., & Gastil, M. (2003). Dual-season mapping of wetland
1019 inundation and vegetation for the central Amazon basin. *Remote Sensing of Environment*, *87*, 404–428. doi:10.
1020 1016/j.rse.2003.04.001.

1021 Huete, A., Liu, H., Batchily, K., & van Leeuwen, W. (1997). A comparison of vegetation indices over a
1022 global set of TM images for EOS-MODIS. *Remote Sensing of Environment*, *59*, 440–451. doi:10.1016/
1023 S0034-4257(96)00112-5.

1024 Hydroweb (). Water height time series available online:. URL: <http://hydroweb.theia-land.fr>
1025 (accessed on 07 July 2022).

1026 Jensen, K., McDonald, K., Podest, E., Rodriguez-Alvarez, N., Horna, V., & Steiner, N. (2018). Assessing L-Band
1027 GNSS-reflectometry and imaging radar for detecting sub-canopy inundation dynamics in a tropicalwetlands
1028 complex. *Remote Sensing*, *10*. doi:10.3390/rs10091431.

1029 Jiménez, C., Catherinot, J., Prigent, C., & Roger, J. (2010). Relations between geological characteristics and
1030 satellite-derived infrared and microwave emissivities over deserts in northern Africa and the Arabian Penin-
1031 sula. *J. Geophys. Res.*, *115*, D20311. doi:10.1029/2010JD013959.

1032 Junk, W. J., Brown, M., Campbell, I. C., Finlayson, M., Gopal, B., Ramberg, L., & Warner, B. G. (2006). The
1033 comparative biodiversity of seven globally important wetlands: a synthesis. *Aquat. Sci.*, *68*, 400–414. doi:10.
1034 1007/s00027-006-0856-z.

1035 Kellndorfer, J., Pierce, L., Dobson, M., & Ulaby, F. (1998). Toward consistent regional-to-global-scale vegetation
1036 characterization using orbital sar systems. *IEEE Transactions on Geoscience and Remote Sensing*, *36*, 1396–1411.
1037 doi:10.1109/36.718844.

1038 Kerr, Y., Waldteufel, P., Wigneron, J.-P., Martinuzzi, J., Font, J., & Berger, M. (2001). Soil moisture retrieval
1039 from space: the Soil Moisture and Ocean Salinity (SMOS) mission. *IEEE Trans. Geosci. Remote Sensing*, *39*,
1040 1729–1735. doi:10.1109/36.942551.

1041 Kim, H., & Lakshmi, V. (2018). Use of Cyclone Global Navigation Satellite System (CyGNSS) Observations for
1042 Estimation of Soil Moisture. *Geophysical Research Letters*, *45*, 11.

1043 Konings, A. G., Piles, M., Das, N., & Entekhabi, D. (2017). L-band vegetation optical depth and effective scatter-
1044 ing albedo estimation from SMAP. *Remote Sensing of Environment*, *198*, 460–470. doi:10.1016/j.rse.
1045 2017.06.037.

1046 Kouadio, I. K., Aljunid, S., Kamigaki, T., Hammad, K., & Oshitani, H. (2012). Infectious diseases following natural
1047 disasters: prevention and control measures. *Expert Review of Anti-infective Therapy*, *10*, 95–104. doi:10.
1048 1586/eri.11.155.

1049 Kreibich, H., Van Loon, A. F., Schröter, K., Ward, P. J., Mazzoleni, M., Sairam, N., Abeshu, G. W., Agafonova,
1050 S., AghaKouchak, A., Aksoy, H. et al. (2022). The challenge of unprecedented floods and droughts in risk
1051 management. *Nature*, (pp. 1–7). doi:10.1038/s41586-022-04917-5.

1052 Kuenzer, C., Guo, H., Huth, J., Leinenkugel, P., Li, X., & Dech, S. (2013). Flood Mapping and Flood Dynamics of
1053 the Mekong Delta: ENVISAT-ASAR-WSM Based Time Series Analyses. *Remote Sensing*, *5*, 687–715. doi:10.
1054 3390/rs5020687.

1055 Lehner, B., & Döll, P. (2004). Development and validation of a global database of lakes, reservoirs and wetlands.
1056 *Journal of Hydrology*, *296*, 1–22. doi:10.1016/j.jhydro1.2004.03.028.

1057 Li, W., Cardellach, E., Fabra, F., Rius, A., Ribó, S., & Martín-Neira, M. (2017). First spaceborne phase altimetry
1058 over sea ice using TechDemoSat-1 GNSS-R signals. *Geophys. Res. Lett.*, *44*, 8369–8376. doi:10.1002/
1059 2017GL074513.

1060 Li, W., CARDELLACH, E., RIBÓ, S., RIUS, A., & ZHOU, B. (2021). First spaceborne demonstration of beidou-3
1061 signals for gnss reflectometry from cygnss constellation. *Chinese Journal of Aeronautics*, 34, 1–10. doi:https :
1062 //doi . org/10 . 1016/j . cja . 2020 . 11 . 016.

1063 Li, W., Cardellach, E., Ribó, S., Oliveras, S., & Rius, A. (2022a). Exploration of multi-mission spaceborne gnss-r
1064 raw if data sets: Processing, data products and potential applications. *Remote Sensing*, 14. doi:10 . 3390/
1065 rs14061344.

1066 Li, X., Wigner, J.-P., Fan, L., Frappart, F., Yueh, S. H., Colliander, A., Ebtehaj, A., Gao, L., Fernandez-Moran, R.,
1067 Liu, X., & al. (2022b). A new SMAP soil moisture and vegetation optical depth product (SMAP-IB): Algorithm,
1068 assessment and inter-comparison. *Remote Sensing of Environment*, 271, 112921. doi:10 . 1016/j . rse .
1069 2022 . 112921.

1070 Loria, E., O'Brien, A., Zavorotny, V., Downs, B., & Zuffada, C. (2020). Analysis of scattering characteristics
1071 from inland bodies of water observed by cygnss. *Remote Sensing of Environment*, 245, 111825. doi:https :
1072 //doi . org/10 . 1016/j . rse . 2020 . 111825.

1073 Macqueen, J. (1967). Some Methods for Classification and Analysis of Multivariate Observations. *Fifth Berkeley*
1074 *Symposium*, (p. 17).

1075 Maltby, E., & Acreman, M. C. (2011). Ecosystem services of wetlands: pathfinder for a new paradigm. *Hydrolog-*
1076 *ical Sciences Journal*, 56, 1341–1359. doi:10 . 1080/02626667 . 2011 . 631014.

1077 Maltby, E., & Immerzi, P. (1993). Carbon dynamics in peatlands and other wetland soils regional and global
1078 perspectives. *Chemosphere*, 27, 999–1023. doi:10 . 1016/0045 - 6535 (93) 90065 -D.

1079 Martin-Neira, M. (1993). *A passive reflectometry and interferometry system (PARIS): application to ocean altimetry*
1080 volume 17. ISSN: 03792285 Publication Title: ESA Journal.

1081 Melton, J. R., Wania, R., Hodson, E. L., Poulter, B., Ringeval, B., Spahni, R., Bohn, T., Avis, C. A., Beer-
1082 ling, D. J., Chen, G., & al. (2013). Present state of global wetland extent and wetland methane mod-
1083 elling: conclusions from a model inter-comparison project (WETCHIMP). *Biogeosciences*, 10, 753–788.
1084 doi:10 . 5194/bg - 10 - 753 - 2013.

1085 Mitra, S., Wassmann, R., & Vlek, P. L. G. (2005). An appraisal of global wetland area and its organic carbon stock.
1086 *Current Science*, 88, 12.

1087 Mitsch, W. J., Bernal, B., Nahlik, A. M., Mander, , Zhang, L., Anderson, C. J., Jørgensen, S. E., &
1088 Brix, H. (2013). Wetlands, carbon, and climate change. *Landscape Ecol*, 28, 583–597. doi:10 . 1007/
1089 s10980 - 012 - 9758 - 8.

1090 Morris, M., Chew, C., Reager, J. T., Shah, R., & Zuffada, C. (2019). A novel approach to monitoring wetland
1091 dynamics using CYGNSS: Everglades case study. *Remote Sensing of Environment*, 233, 111417. doi:10.1016/
1092 j.rse.2019.111417.

1093 Müller, M. (2007). Dynamic Time Warping. In M. Müller (Ed.), *Information Retrieval for Music and Motion* (pp.
1094 69–84). Berlin, Heidelberg: Springer Berlin Heidelberg. doi:10.1007/978-3-540-74048-3_4.

1095 Nisbet, E. G., Dlugokencky, E. J., & Bousquet, P. (2014). Methane on the Rise—Again. *Science*, 343, 493–495.
1096 doi:10.1126/science.1247828.

1097 Normandin, C., Frappart, F., Lubac, B., Bélanger, S., Marieu, V., Blarel, F., Robinet, A., & Guiastrennec-Faugas, L.
1098 (2018). Quantification of surface water volume changes in the Mackenzie Delta using satellite multi-mission
1099 data. *Hydrol. Earth Syst. Sci.*, 22, 1543–1561. doi:10.5194/hess-22-1543-2018.

1100 Page, S. E., Rieley, J. O., & Banks, C. J. (2011). Global and regional importance of the tropical peatland carbon
1101 pool. *Global Change Biology*, 17, 798–818. doi:10.1111/j.1365-2486.2010.02279.x.

1102 Parrens, M., Al Bitar, A., Frappart, F., Papa, F., Calmant, S., Crétaux, J.-F., Wigneron, J.-P., & Kerr, Y. (2017). Map-
1103 ping Dynamic Water Fraction under the Tropical Rain Forests of the Amazonian Basin from SMOS Brightness
1104 Temperatures. *Water*, 9, 350. doi:10.3390/w9050350.

1105 Pekel, J.-F., Cottam, A., Gorelick, N., & Belward, A. S. (2016). High-resolution mapping of global surface water
1106 and its long-term changes. *Nature*, 540, 418–422. doi:10.1038/nature20584.

1107 Prigent, C., Aires, F., Jimenez, C., Papa, F., & Roger, J. (2015). Multiangle Backscattering Observations of Conti-
1108 nental Surfaces in Ku-Band (13 GHz) From Satellites: Understanding the Signals, Particularly in Arid Regions.
1109 *IEEE Trans. Geosci. Remote Sensing*, 53, 1364–1373. doi:10.1109/TGRS.2014.2338913.

1110 Prigent, C., Jimenez, C., & Bousquet, P. (2020). Satellite-Derived Global Surface Water Extent and Dynamics
1111 Over the Last 25 Years (GIEMS-2). *J. Geophys. Res. Atmos.*, 125. doi:10.1029/2019JD030711.

1112 Prigent, C., Matthews, E., Aires, F., & Rossow, W. B. (2001). Remote sensing of global wetland dynamics with
1113 multiple satellite data sets. *Geophys. Res. Lett.*, 28, 4631–4634. doi:10.1029/2001GL013263.

1114 Prigent, C., Papa, F., Aires, F., Rossow, W. B., & Matthews, E. (2007). Global inundation dynamics inferred from
1115 multiple satellite observations, 1993–2000. *J. Geophys. Res.*, 112, D12107. doi:10.1029/2006JD007847.

1116 Rajabi, M., Nahavandchi, H., & Hoseini, M. (2020). Evaluation of CYGNSS Observations for Flood Detec-
1117 tion and Mapping during Sistan and Baluchestan Torrential Rain in 2020. *Water*, 12, 2047. doi:10.3390/
1118 w12072047.

1119 Richards, J. A., Woodgate, P. W., & Skidmore, A. K. (1987). An explanation of enhanced radar backscat-
1120 tering from flooded forests. *International Journal of Remote Sensing*, 8, 1093–1100. doi:10.1080/
1121 01431168708954756.

- 1122 Ringeval, B., de Noblet-Ducoudré, N., Ciais, P., Bousquet, P., Prigent, C., Papa, F., & Rossow, W. B. (2010). An
1123 attempt to quantify the impact of changes in wetland extent on methane emissions on the seasonal and
1124 interannual time scales. *Global Biogeochem. Cycles*, *24*. doi:10.1029/2008GB003354.
- 1125 Rodriguez-Alvarez, N., Podest, E., Jensen, K., & McDonald, K. C. (2019). Classifying Inundation in a Tropical
1126 Wetlands Complex with GNSS-R. *Remote Sensing*, *11*, 1053. doi:10.3390/rs11091053.
- 1127 Rousseeuw, P. J. (1987). Silhouettes: A graphical aid to the interpretation and validation of cluster analysis.
1128 *Journal of Computational and Applied Mathematics*, *20*, 53–65. doi:10.1016/0377-0427(87)90125-7.
- 1129 Ruf, C. S., Atlas, R., Chang, P. S., Clarizia, M. P., Garrison, J. L., Gleason, S., Katzberg, S. J., Jelenak, Z., Johnson,
1130 J. T., Majumdar, S. J., O'Brien, A., Posselt, D. J., Ridley, A. J., Rose, R. J., & Zavorotny, V. U. (2016). New ocean
1131 winds satellite mission to probe hurricanes and tropical convection. *Bulletin of the American Meteorological*
1132 *Society*, *97*, 385–395. doi:10.1175/BAMS-D-14-00218.1.
- 1133 Ruffini, G., Soulat, F., Caparrini, M., Germain, O., & Martín-Neira, M. (2004). The Eddy Experiment: Accurate
1134 GNSS-R ocean altimetry from low altitude aircraft. *Geophys. Res. Lett.*, *31*. doi:10.1029/2004GL019994.
- 1135 Russo, I. M., Bisceglie, M. d., Galdi, C., Lavallo, M., & Zuffada, C. (2022). Entropy-based coherence metric for
1136 land applications of gnss-r. *IEEE Transactions on Geoscience and Remote Sensing*, *60*, 1–13. doi:10.1109/
1137 TGRS.2021.3125858.
- 1138 Sakamoto, T., Van Nguyen, N., Kotera, A., Ohno, H., Ishitsuka, N., & Yokozawa, M. (2007). Detecting temporal
1139 changes in the extent of annual flooding within the Cambodia and the Vietnamese Mekong Delta from MODIS
1140 time-series imagery. *Remote Sensing of Environment*, *109*, 295–313. doi:10.1016/j.rse.2007.01.011.
- 1141 Santoro, M. (2018). GlobBiomass - global datasets of forest biomass. doi:10.1594/PANGAEA.894711.
- 1142 Santoro, M., Cartus, O., Carvalhais, N., Rozendaal, D. M. A., Avitabile, V., Araza, A., de Bruin, S., Herold, M.,
1143 Quegan, S., Rodríguez-Veiga, P., Balzter, H., Carreiras, J., Schepaschenko, D., Korets, M., Shimada, M., Itoh, T.,
1144 Moreno Martínez, A., Cavlovic, J., Cazzolla Gatti, R., da Conceição Bispo, P., Dewnath, N., Labrière, N., Liang,
1145 J., Lindsell, J., Mitchard, E. T. A., Morel, A., Pacheco Pascagaza, A. M., Ryan, C. M., Slik, F., Vaglio Laurin,
1146 G., Verbeeck, H., Wijaya, A., & Willcock, S. (2021). The global forest above-ground biomass pool for 2010
1147 estimated from high-resolution satellite observations. *Earth System Science Data*, *13*, 3927–3950. doi:10.
1148 5194/essd-13-3927-2021.
- 1149 Saunio, M., Stavert, A. R., Poulter, B., Bousquet, P., Canadell, J. G., Jackson, R. B., Raymond, P. A., Dlugokencky,
1150 E. J., Houweling, S., Patra, P. K., & al. (2020). The global methane budget 2000–2017. *Earth System Science*
1151 *Data*, *12*, 1561–1623. doi:10.5194/essd-12-1561-2020.

1152 Senyurek, V., Lei, F., Boyd, D., Kurum, M., Gurbuz, A. C., & Moorhead, R. (2020). Machine learning-based
1153 CYGNSS soil moisture estimates over ISMN sites in CONUS. *Remote Sensing*, *12*, 1–24. doi:10.3390/
1154 rs12071168.

1155 Sippel, S. J., Hamilton, S. K., Melack, J. M., & Choudhury, B. J. (1994). Determination of inundation area in the
1156 Amazon River floodplain using the SMMR 37 GHz polarization difference. *Remote Sensing of Environment*, *48*,
1157 70–76. doi:10.1016/0034-4257(94)90115-5.

1158 Suk, J. E., Vaughan, E. C., Cook, R. G., & Semenza, J. C. (2020). Natural disasters and infectious disease in
1159 Europe: a literature review to identify cascading risk pathways. *European Journal of Public Health*, *30*, 928–
1160 935. doi:10.1093/eurpub/ckz111.

1161 Tavenard, R., Faouzi, J., Vandewiele, G., Divo, F., Androz, G., Holtz, C., Payne, M., Yurchak, R., Rußwurm, M.,
1162 Kolar, K., & Woods, E. (2020). Tslearn, A Machine Learning Toolkit for Time Series Data. *Journal of Machine*
1163 *Learning Research*, *21*, 1–6.

1164 Tootchi, A., Jost, A., & Ducharne, A. (2019). Multi-source global wetland maps combining surface water imagery
1165 and groundwater constraints. *Earth Syst. Sci. Data*, *11*, 189–220.

1166 Ulaby, F., Moore, R., & Fung, A. (1982). Microwave remote sensing: Active and passive. volume 2-radar remote
1167 sensing and surface scattering and emission theory, .

1168 Unwin, M. J., Pierdicca, N., Cardellach, E., Rautiainen, K., Foti, G., Blunt, P., Guerriero, L., Santi, E., & Tossaint, M.
1169 (2021). An introduction to the hydrognss gns reflectometry remote sensing mission. *IEEE Journal of Selected*
1170 *Topics in Applied Earth Observations and Remote Sensing*, *14*, 6987–6999. doi:10.1109/JSTARS.2021.
1171 3089550.

1172 Wan, W., Liu, B., Zeng, Z., Chen, X., Wu, G., Xu, L., Chen, X., & Hong, Y. (2019). Using CYGNSS Data to Monitor
1173 China’s Flood Inundation during Typhoon and Extreme Precipitation Events in 2017. *Remote Sensing*, *11*, 854.
1174 doi:10.3390/rs11070854.

1175 Webb, E. B., Smith, L. M., Vrtiska, M. P., & Lagrange, T. G. (2010). Effects of Local and Landscape Variables on
1176 Wetland Bird Habitat Use During Migration Through the Rainwater Basin. *Journal of Wildlife Management*,
1177 *74*, 109–119. doi:10.2193/2008-577.

1178 Whalen, S. (2005). Biogeochemistry of Methane Exchange between Natural Wetlands and the Atmosphere.
1179 *Environmental Engineering Science*, *22*, 73–94. doi:10.1089/ees.2005.22.73.

1180 Wigneron, J.-P., Li, X., Frappart, F., Fan, L., Al-Yaari, A., De Lannoy, G., Liu, X., Wang, M., Le Masson, E., &
1181 Moisy, C. (2021). SMOS-IC data record of soil moisture and L-VOD: Historical development, applications and
1182 perspectives. *Remote Sensing of Environment*, (p. 20).

- 1183 Xiao, X., Boles, S., Liu, J., Zhuang, D., Frohking, S., Li, C., Salas, W., & Moore, B. (2005). Mapping paddy rice
1184 agriculture in southern China using multi-temporal MODIS images. *Remote Sensing of Environment*, 95, 480–
1185 492. doi:10.1016/j.rse.2004.12.009.
- 1186 Yan, Q., Huang, W., Jin, S., & Jia, Y. (2020). Pan-tropical soil moisture mapping based on a three-layer model
1187 from CYGNSS GNSS-R data. *Remote Sensing of Environment*, 247, 111944. doi:10.1016/j.rse.2020.
1188 111944.
- 1189 Zavorotny, V. U., Gleason, S., Cardellach, E., & Camps, A. (2014). Tutorial on remote sensing using GNSS bistatic
1190 radar of opportunity. *IEEE Geoscience and Remote Sensing Magazine*, 2, 8–45. doi:10.1109/MGRS.2014.
1191 2374220. Publisher: IEEE.